Active Sensor Array for UWB Breast-Cancer Screening

ACTIVE SENSOR ARRAY FOR UWB BREAST-CANCER SCREENING

BY

VARTIKA TYAGI

A THESIS

SUBMITTED TO THE DEPARTMENT OF

ELECTRICAL & COMPUTER ENGINNERING

AND THE SCHOOL OF GRADUATE STUDIES

IN PARTIAL FULFILMENT OF THE

REQUIREMENTS FOR THE DEGREE OF MASTER

OF APPLIED SCIENCE

McMaster University

Master of Applied Science (2021)

Hamilton, Ontario (Department of Electrical & Computer Engineering)

TITLE: Active Sensor Array for UWB Breast-Cancer Screening

AUTHOR: Vartika Tyagi

SUPERVISORS: Dr. Natalia K. Nikolova, Dr. Chih-Hung (James) Chen

NUMBER OF PAGES: xiii, 93

Abstract

A microwave imaging system processes scattered electromagnetic fields in the microwave region to create images. It is an alternative or complementary imaging tool that can be used in breast cancer imaging. It employs non-ionising radiation and during measurement, compression of the scanned body part is avoided. These benefits potentially lead to safer and more comfortable examinations. It also has the potential to be both sensitive and specific to detect small tumors, whilst being much lower cost than current methods, such as magnetic resonant imaging, mammography and ultrasound. This thesis reports a multi-layer active antenna array for breast imaging using microwaves from 3 GHz to 8 GHz. The proposed structure resolves the outstanding problem in the design of large active antenna arrays for tissue imaging, namely, the isolation of the antennas from the electronic circuits. A ground plane within the multi-layer design separates the antenna array from the electronics array while providing shielding to the antennas from the back and improved power coupling into the tissue. The possibility of a high-speed vertical connector to provide interconnection between the antenna array and the mixer array is investigated and measurements show that it could be utilized for the frequency range from 3 GHz to 8 GHz.

To my parents

Acknowledgements

I would like to begin by expressing my sincere gratitude to my supervisor Prof. Natalia K. Nikolova for her continuous support, and patience throughout my research. She has been a source of motivation with her immense knowledge and zeal. Her guidance kept me going in all the times during my research and writing of this thesis. She not only extended her support academically, but also emotionally. I could not have asked for a better supervisor and mentor for this journey. I am also indebted to my co-supervisor, Prof. Chih-Hung (James) Chen, for his constant encouragement and insightful comments for my research and this thesis.

A big shout out to all the wonderful members of the *EMVi* lab. This group is a collection of amazing and extraordinary individuals. I am grateful for all the help I received over the years of my study. Our team's get-togethers and Prof. Nikolova's parties will be missed.

This acknowledgement would be far from complete, without me extending my deepest thanks to my beautiful daughter Naysha for enduring years of tasteless food without complaining and countless 'just give me a few more minutes to work' moments that actually never lasted a few minutes. Varun Tyagi thanks for being my strength, without you this would not have been possible.

Contents

List of Figures

List of Tables

Chapter 1

Introduction

Breast cancer is one of the most prevalent and deadliest types of cancer among women worldwide. For the year 2020, the Canadian Cancer Society estimated that 27,400 women would be diagnosed with breast cancer [1]. This represents 25% of all new cancer cases in women in 2020. Detecting breast cancer during its early stages, is critical for successful treatment. The most common clinical imaging and detection modalities used for breast cancer detection currently are X-ray mammography, magnetic resonance imaging (MRI), and ultrasound [2].

Mammography is the most widely used for breast cancer screening in women with no prior symptoms. Mammography, however, has recently been scrutinized because of relatively high false-negative results [3]. Furthermore, women who use mammography as a screening test may have a higher chance of developing cancer because of the ionizing X-ray radiation [4], [5]. Physical discomfort due to significant compression is another drawback of this imaging technique. Ultrasound screening is another technique of breast cancer detection. However, it exhibits low resolution and is operator dependent and therefore, it is only employed as a complementary technique [6], [7]. MRI is highly sensitive in detecting invasive and small abnormalities compared with mammography and ultrasound techniques and can be used effectively for patients with dense breasts. Testing with MRI, however, is relatively expensive and requires a contrast agent [8]. These factors make it unsuitable for mass screening.

The disadvantages and limitations of the current breast cancer screening techniques motivated researchers to investigate and develop new imaging modalities, including those based on microwaves. The concept of using microwaves for breast cancer detection received significant attention and extensive investigations due to several advantages, including low cost, non-ionizing radiation, no discomfort, and wide access (once implemented) compared with the existing techniques. In addition, the microwave imaging (MI) method provides sufficient sensitivity for the purposes of screening and has the ability to detect small sub-centimeter breast tumours based on the electrical properties' contrast between normal and malignant breast tissues [9].

1.1 Microwave imaging for breast cancer detection

The fundamental premise of microwave imaging is the presence of contrast in the dielectric properties of cancerous tissues in comparison to healthy tissues. Knowledge of the dielectric properties of breast tissues is essential for the understanding of the interaction between microwave radiation and breast tissue. The dielectric properties of breast tissues are represented by a complex permittivity where the real part represents the ability of the material to store microwave energy, whereas the imaginary part, or the loss factor, indicates the ability of the material to absorb microwave energy. Microwave-based detection modalities are mainly based on the observation of the differences in the dielectric properties of normal and malignant breast tissues [10]. Microwaves reflected or scattered from breast tissues are processed to obtain an image showing the contrast between malignant and healthy tissues. Several research groups studied the dielectric properties of normal and malignant breast tissues in the microwave region [11–19]. The accuracy of the differences between the normal and tumorous tissues of each reported study is based on many factors such as the frequency range for the fitting model, tissue type and size, number of samples used for the study, sensing depth and volume, time from excision to the measurement, type of the fitting data model used, and the environment of testing (i.e., *in vivo* or *ex vivo* states). For example, in [9] and [13], a small number of sam-

ples (patients) were used. Also, a small range of frequencies not exceeding 3.2 GHz was employed, which resulted in inaccurate difference estimation between the three types of tissues, namely, normal, benign, and malignant breast tissues. The studies at the University of Wisconsin and the University of Calgary reported the dielectric properties of normal, benign, and malignant breast tissues within an ultra-wideband frequency range. The results, in general, confirm a contrast between the healthy and cancerous breast tissue. The study reported in [16] introduced the differences in dielectric properties between *in vivo* and *ex vivo* states of breast tissues. However, this study considered a small sample of six women. The studies reported in [17], [18], and [19] used larger samples and a wide range of frequencies for measuring the differences between the dielectric properties of normal and tumorous tissues. Fig. 1.1 shows the frequency spectra of both dielectric constant and conductivities reported by Sugitani *et al.* [17].

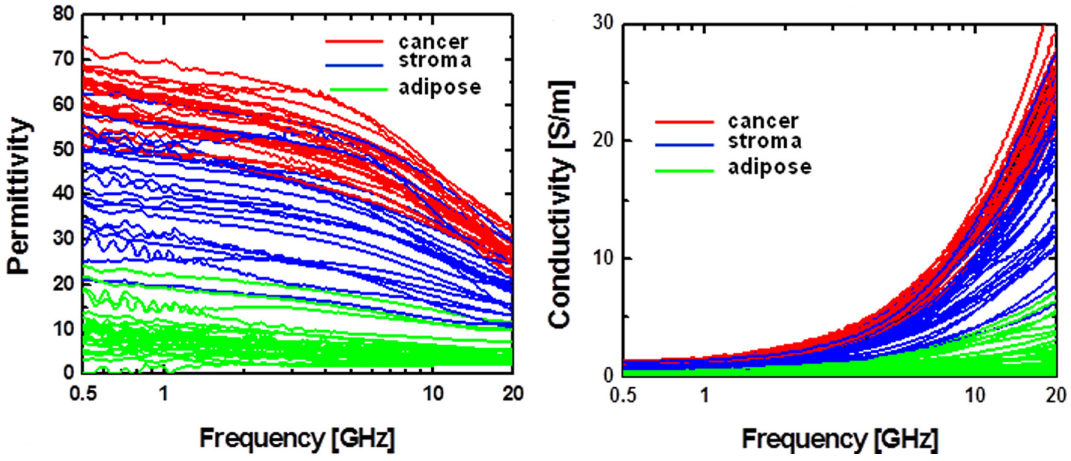

(a) (b)

Fig. 1.1. Frequency spectra of dielectric constants and conductivities of freshly excised breast cancer, stroma, and adipose tissues. (a) Dielectric constant versus frequency. (b) Conductivity versus frequency [17].

The following observations could be made based on these studies. Firstly, the constitutive parameters of both the cancerous tissue and the healthy tissue are frequency-dependent. Secondly, the parameters of the normal tissue show considerable variations from patient to patient and between the different types of healthy tissue, e.g., between the fatty and the fibroglandular tissue. Finally, all except the fattiest breast

tissues have considerable losses (as indicated by the increased conductivity), and the losses increase with frequency. This should all be kept in mind when developing microwave imaging systems for breast cancer screening.

Microwave imaging systems have come a long way since the first experiments conducted by Larsen and Jacobi in the 1970s, in which they successfully produced two-dimensional (2-D) images of canine kidneys [20], [21]. Various research groups around the world have since developed a number of imaging systems utilizing microwaves. In most fundamental form, microwave imaging can be understood using Fig. 1.2. The background medium, in which the microwave imaging system is embedded, is characterized by the permittivity ε_{bg} and conductivity σ_{bg} and the area in the center of the antenna array represents the imaging domain. This domain is irradiated by a transmitting antenna, and the total field is measured by one or more antennas positioned outside the domain. When an object with contrast in the constitutive parameters is positioned inside the imaging domain, a scattered field arises. The total field, measured by the receiving antennas, is the sum of the incident field and the scattered field as given by:

$$\mathbf{E}_{\text{tot}} = \mathbf{E}_{\text{inc}} + \mathbf{E}_{\text{sc}}. \tag{1.1}$$

From the information contained within $\mathbf{E}_{\text{sc}}$, location and/or constitutive parameters of the scattering object can be obtained.

Various microwave imaging setups, modalities, and algorithms exist for extracting information from measurements of the total field. The most simple measurement setup is the monostatic one, in which the same antenna is used both for transmitting the incident field and for measuring the resulting total field. Additional information about the scatterer may be obtained by moving the transmitting/receiving antenna to different positions, a technique known as multi-monostatic measurements [22], [23], [24]. Ground-penetrating radar is a major application of microwave imaging [22], [25], [26], and in it the multi-bistatic setup is widely used. In this

configuration, two antennas are used; one is transmitting, the other one receiving, hence the term bistatic. This pair of antennas may then be moved around the imaged domain to obtain information about the scattering objects from multiple transmit-receive positions. The last type of commonly used measurement setup is the multistatic setup in which several antennas are used. At any given time, one antenna transmits and all the others receive, providing a large number of spatial variations of the measurements [27], [28], [29].

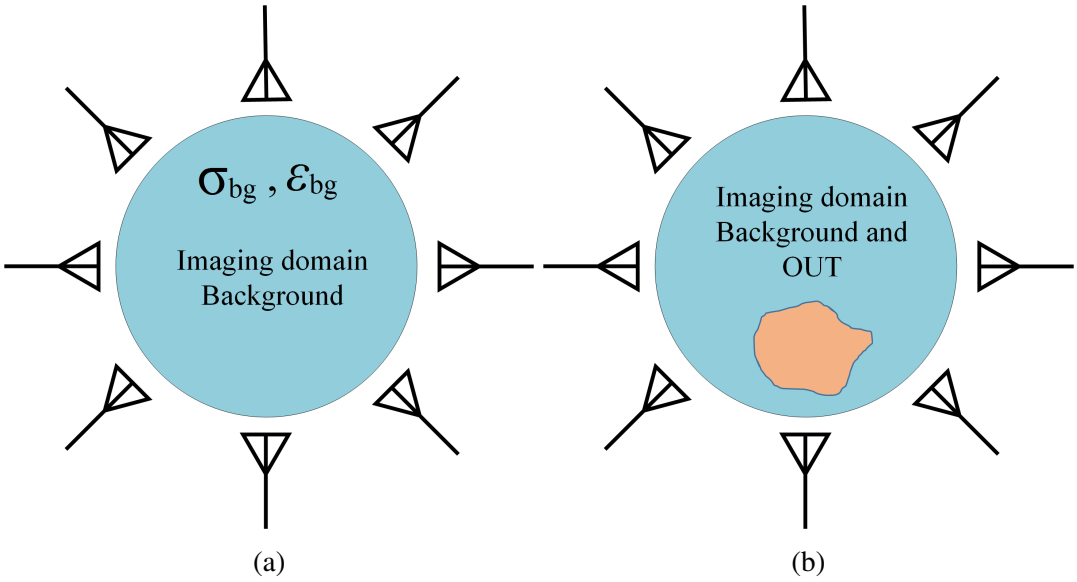

Fig. 1.2. Schematic of a microwave imaging system. A known incident field is transmitted into the background medium by one antenna, and the response is measured by one or more receiving antennas. When an object with constitutive parameters different from those of the background is present in the imaging domain, scattered field arises, and the total field measured by the antennas is the sum of the incident and the scattered field.

1.2 Challenges in the design and development of microwave imaging systems for clinical applications

Most of the challenges in designing a microwave imaging system stem from the interaction between microwaves and tissues. In this section, we look into some of the issues that need to be addressed, both in terms of antenna design and processing algorithms, in order to attain acceptable images.

1.2.1 Coupling of microwave power in tissues and incurred losses

From section 1.1, it is clear that the electrical properties of breast tissues are highly diverse and are very different from the surrounding environment. A lot of incident power is lost at the skin-air interface. The incident power is further attenuated by the layers of fat and fibroglandular tissue in the breast due to reflections and dissipation. Additionally, the properties are frequency-dependent, as shown in Fig.1.1. This feature is attributed to the high water content in the tissues. To mitigate such strong signal attenuation, coupling liquids are used, as reported in [20], [21], which reduce the large dielectric difference between the antenna environment and the breast. Moreover, the same acquisition setup can be used for body parts of various sizes. However, this approach presents certain limitations, such as cross-contamination among patients and losses in the coupling medium. Also, some of the incident field misses the object under test (OUT).

Another approach to coupling the microwave power into the tissue is the direct contact between the OUT and antenna elements. This, in theory, reduces power wastage. Such systems feature higher sensitivity, which is defined by the weakest signal that the system can detect. Better sensitivity leads to a higher dynamic range and the detection of smaller targets. This, however, puts a lot of strain on the system design, as smaller size antenna elements are required, which must have good impedance matching in the whole frequency band of interest, which is usually very wide. In addition to this, the system must adjust to any shape and size.

As mentioned previously, the various breast tissues, like skin, fat, and fibrograndular, show different conductivities. Moreover, these properties vary with frequencies. As reported in [30], at 10 GHz within few centimeters, the signal is attenuated by as much as 80 dB. It is expected that the received signal could be weaker than the incident signal by a value of -100 dB. The imaging systems should be able to detect such weak signals, which in fact, is a very difficult task. Modern vector network analyzers (VNA) can detect signals as low as -140 dB. However, this involves a lot of system calibration and also increases the acquisition time.

1.2.2 Optimal frequency range

The optimal choice of the frequency range of operation is another challenge. For better penetration of the microwaves into the tissues, lower frequencies are preferred. Higher frequencies, on the other hand, are required to obtain a sub-centimeter resolution of the reconstructed images. To satisfy both of the requirements, a large fractional bandwidth is needed, and therefore UWB systems are attractive for imaging applications. The use of UWB for microwave imaging of the breast was first reported by Hagness *et al.* [31] and Fear *et al.* [32], who applied both multi-monostatic and multistatic imaging systems. Following these preliminary studies, several research groups have published results using UWB radar approaches [33], [34], [35], [36], [37]. A common feature in these systems is the use of a coupling liquid for reducing the contrast between the background and the breast, thereby maximizing the amount of energy coupled to the interior of the breast.

It has been observed that the frequency range between 0.5 GHz to 3 GHz and 2 GHz to 8 GHz are the most suitable for breast imaging [10], [38], [39]. However, the choice of the frequency band is largely influenced by the used reconstruction algorithm. The imaging algorithm most frequently applied for UWB systems, typically operating between 3 GHz and 8 GHz, is the confocal or delay-and-sum imaging algorithm [31], [35], [36], [34], a technique that has been used in synthetic aperture radar for many years. This type of algorithm assumes that the scattering effects are due to point scatterers [40] and that the scattered fields from the individual point scatterers do not interact with other scatterers in the imaging domain. Hence, the imaging problem is solved as a linear inverse problem. In addition to the UWB imaging systems, nonlinear inverse scattering, also known as microwave tomography, has been reported for microwave imaging of the breast [41], [28]. These approaches can achieve spatial resolution as fine as one-tenth of the wavelength, and the frequency used could be as low as 300 MHz [28]. Other imaging systems work with single frequencies as reported in [42], where 2.45 GHz is the chosen frequency.

1.2.3 Microwave imaging setup

For the longest time, mechanical scanning has been used in the imaging of the breast to ensure sufficiently dense spatial sampling [43], [44], [45], [46]. An example of a planar raster-scanned system is shown in Fig. 1.3. The photo shows the planar raster-scanning data acquisition set-up at McMaster University [43]. An in-house TEM horn antenna reported in [45] is used to transmit, and an in-house array of nine bow-tie antennas is employed as the receiving array. In the receiving array design, out of the nine elements, five are co-polarized with the transmitting antenna, and the remaining four elements are cross-polarized. An area of 14×14 cm^2 is scanned with a step size of 3 mm, both in the x and y directions. Frequency sampling of 100 MHz step size is employed from 3 GHz to 8 GHz. The measurements on these systems take a very long time, typically hours. Such long acquisition times are unacceptable in a clinical setting and, therefore, fast electronically switched acquisition systems are necessary. Also, these systems suffer from positioning errors which impact negatively the image quality. Electronically switched arrays are superior to mechanical

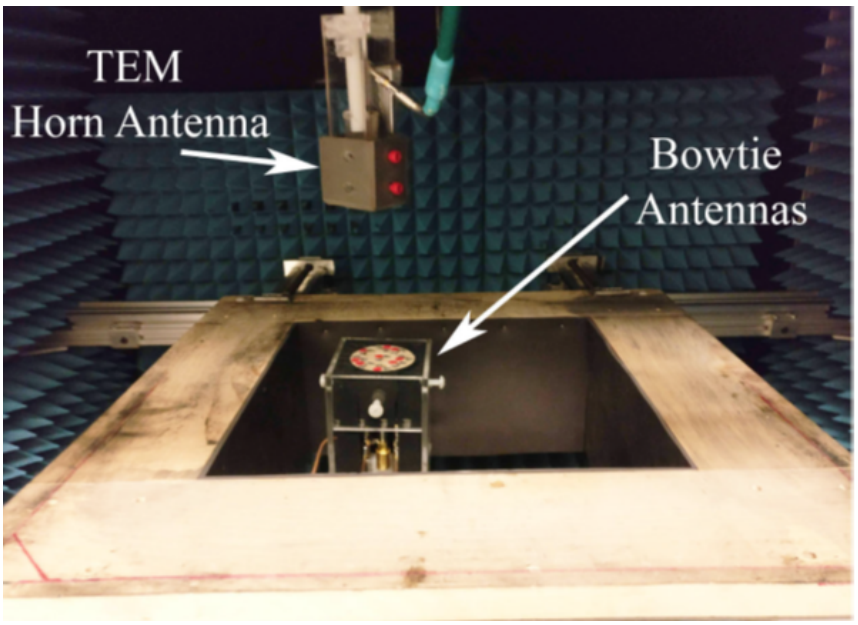

Fig. 1.3. Planar scanning setup at McMaster University. The TEM horn antenna for transmission and the receiving bow-tie antenna array can be observed in the photo [43].

scanning both in terms of speed and positioning errors [47], [48]. Mechanical scan-

ning offers flexibility in the choice of sampling steps and patterns, which is desirable in initial research and system development. Yet, it must ultimately be transferred onto an electronically switched platform. In the electronically switched systems, the array of antennas allows for multi-static measurements, where, at any given time, one antenna transmits and all others receive. RF switching networks are used to multiplex both the transmitting and the receiving antennas connected to the ports of a vector network analyzer. However, RF switching has drawbacks such as substantial insertion loss, high cost, interconnect complexity, and difficulties with system calibration.

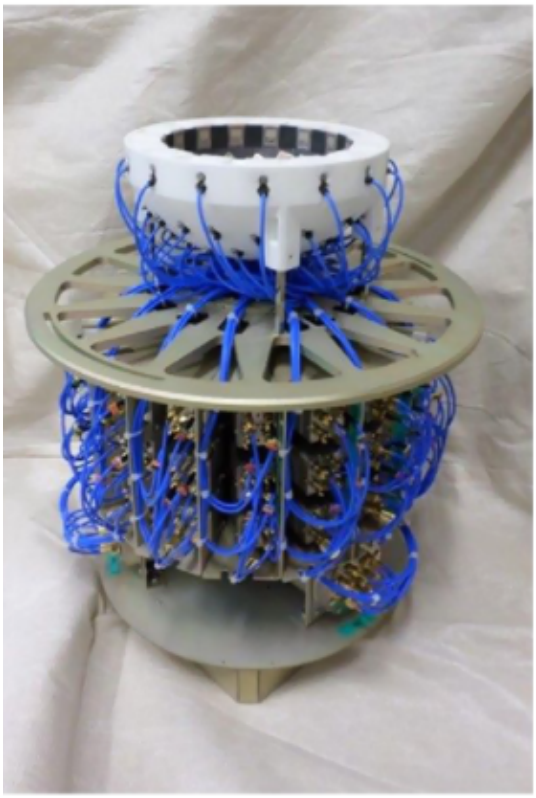

Fig. 1.4. MARIA M4/M5 array with 60 antennas and switch assembly, [48].

Also, current off-the-shelf RF switches do not provide large enough numbers of ports. Typical RF switches for high-quality wideband VNA measurements offer up to 16 multiplexed ports. In comparison, the mechanically scanned system shown in Fig. 1.3 provides 12,500 spatial samples when only the co-polarized receiving antennas are used. Current RF switches cannot multiplex such a large number of

ports. To our best knowledge, the breast-scanning system with the largest number of RF switched ports currently is MARIA M4, developed at the University of Bristol, which uses 60 RF switched antennas as shown in Fig.1.4. To overcome the limitation on sampling with fixed antenna arrays, RF switching is often augmented by additional mechanical scanning. For example, in [49], a hand-held compact impulse-radar detector is developed using a 4×4 cross-shaped dome antenna array. Two single-pole-eight-throw (SP8T) RF switches are used to control the antenna array elements. In addition to the antenna element switching, rotation is employed in order to obtain sufficient spatial sampling.

To deal with the above mentioned limitation of RF switching systems, the modulated scatterer technique (MST) has been proposed, which replaces the RF switching networks with arrays of electronically modulated scattering-probe arrays, allowing for fast sampling over thousands of spatial points [50], [51], [52], [53]. The method, however, has limited dynamic range and frequency bandwidth both of which adversely affect the image quality.

In the system architecture considered later in this thesis, the channel multiplexing is done at the intermediate frequency (IF), where a channel provides a single-tone low-frequency signal. Such narrow-band low-frequency channels can be multiplexed with an in-house network of on-chip IF switches. This system architecture aims to address the limitations of the existing electronically switched systems for microwave imaging.

1.3 Contributions to the knowledge

The work undertaken in this thesis has contributed to the development of a microwave imaging system for breast-cancer screening as follows:

1. A planar multi-layer active sensor array is developed to work in direct contact with the body. The distinguishable feature of this prototype is the complete isolation of the electronic components from the antenna using a shield. The

signal from the antenna is vertically transferred through a triple-via transition to the top layer, housing the electronics.

2. A vertical high-speed connector is characterized to validate its performance in the frequency range from 3 GHz to 8 GHz. The connector is investigated to provide inter-connectivity between the antenna array board and the mixer array board.

1.4 Thesis outline

In chapter 2, a brief overview of the envisioned system at McMaster University is presented. An electronically switched system is proposed in which the output is taken at an intermediate frequency (IF). The steps in the design and development of each module, such as transmitting and receiving antenna arrays and the active sensors are outlined.

In chapter 3, the novel antenna array design with vertical transition is presented. This design is developed to overcome the drawbacks of the previous design reported in [54]. The chapter also presents the simulation and measurement results of the developed prototype.

In chapter 4, the measurement results of the high-speed vertical connector are presented. This connector is being investigated, in order to connect the planar active antenna array to the mixer-array board.

In chapter 5, recommendations for future work are given towards the completion of the proposed architecture. Concluding remarks are also given.

Chapter 2

Background: Envisioned System Architecture for Planar Breast Scanning

Microwave imaging systems have evolved over the past several decades, and many of these systems were prototyped [47, 48, 55, 56]. However, to our knowledge, none of these proceeded beyond the pilot clinical trials. One of the likely reasons is the insufficient diagnostic accuracy. In most medical imaging modalities, patient movement coupled with positioning errors can lead to significant measurement uncertainties, which result in image degradation. Designing an acquisition system to minimize these errors is crucial in order to produce high-quality images. Moreover, intrinsic system limitations, such as low signal-to-noise ratio (SNR) and small dynamic range, have a detrimental impact on the image spatial and property resolution. These limitations are present regardless of the geometry of the desired acquisition surface or the algorithms used to reconstruct the images.

2.1 System architecture

As discussed in Chapter 1, the RF switched systems have minimal positioning errors and much faster acquisition time in comparison with the mechanically scanned

systems. However, they cannot provide the desired large number of multiplexed ports due to losses, unequal signal delays, and reliability problems due to poor contact, bending of cables, or leakage. The modulated scatterer technique [50–53], on the other hand, is capable of multiplexing a large number of ports, but has a limited dynamic range (to about 30 dB). The challenge is to design and develop a new imaging system architecture that could circumvent the limitations of the existing techniques.

The architecture discussed in this chapter is an electronically-switched active sensor array for tissue imaging; see Fig. 2.1. Each element of the receiving antenna array is coupled with a front-end receiver. The received radio-frequency (RF) power is down-converted to an intermediate frequency (IF) right at the antenna terminals, which avoids the complicated switching and power splitting networks at the RF frequencies. The working principles of the system architecture are discussed next.

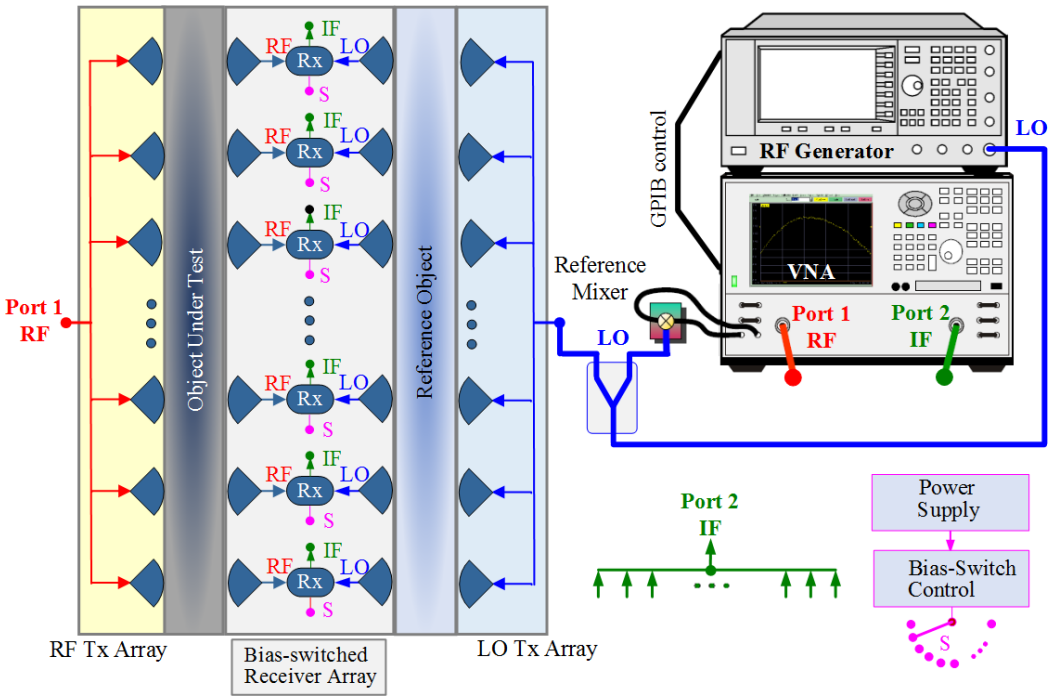

Fig. 2.1. The System architecture of the breast-imaging prototype consisting of: a vector network analyzer (VNA) (in converter-measurement mode), RF generator, reference mixer, and the imaging module. The imaging module consists of: (a) RF transmitting (Tx) array; (b) local oscillator (LO) Tx array; (c) RF receiving (Rx) active-antenna array, (d) LO Rx active-antenna array, and (e) array of ultra-wideband (UWB) receivers between the RF and LO active-antenna arrays [57].

The components of the envisioned system architecture are shown in Fig. 2.1. The system along with the imaging module consists of a 2-port vector network analyzer (VNA), an auxiliary RF generator, and a reference mixer circuit. The imaging module employs four antenna arrays: (a) RF transmitting (Tx) array fed by the VNA through a power-distribution network; (b) the local oscillator (LO) Tx array fed by the synchronized RF generator; (c) the RF receiving (Rx) active array that captures the scattered signals through the object under test; and (d) the LO Rx active array that receives the LO frequency signal through the reference object. The passive antenna elements of all four arrays are the same. The system envisions an 18×18 antenna array. The spatial sampling of the system is determined by the inter-element spacing. The current spacing with the antenna array prototype reported in [54] is 12 mm, which can provide a maximum scanned area of 204×204 mm^2. Each of the active antennas in the receiving arrays is equipped with a low-noise amplifier. The signals from both the RF and LO Rx arrays are fed into the ultra-wideband (UWB) receivers (LNA and mixers), which down-convert the signals from the RF band (ranging from 3 GHz to 8 GHz) to the IF of either 10 MHz or 30 MHz, depending on the prototype implementation.

The IF outputs are received at port 2 of the VNA through a network of IF switches. For improved channel de-coupling, a bias-switching network works synchronously with the IF switches. It turns ON the DC bias of the receiver only for the active antenna element whose IF switch is ON. At any given measurement, only one receiver is powered, and all others are muted, not only through the lack of biasing power but also through the IF switching network. Moreover, the IF switches ensure impedance match between the activated ultra-wideband receiver and the 50 Ohm IF system output at the VNA, whereas all other UWB receivers, which are in the OFF state, are impedance-mismatched (disconnected). The purpose of this switching architecture is to ensure a large dynamic range (typically better than 100 dB) at the IF system output, where the maximum signal strength is limited only by the mixer's 1-dB compression point whereas the system noise floor (the combined output of all radios in the OFF state) is at or below the noise floor of the VNA. It also ensures minimal

channel interference (good isolation) between the receivers in the OFF state and the receiver in the ON state. The IF outputs are received at port 2 of the VNA that is configured for "converter" measurements, which provide conversion parameters with both magnitude and relative phase at IF within a dynamic range comparable to that in the normal S-parameter mode of operation. This system takes advantage of the large dynamic range and frequency bandwidth of a VNA along with the speed of electronic switching. Multiplexing of hundreds of sensors becomes feasible by combining digital DC-bias and IF-output switching networks. These networks are as fast as RF switching but they feature negligible signal loss and distortion. They use low-cost, reliable chip technology, thus avoiding low interconnect reliability and extremely cumbersome calibration.

2.2 Development stages of the imaging module of the architecture

This section focuses on the development of the different segments of the imaging module, namely, the transmitting antenna arrays, active receiving arrays, and the mixers (or radios). Also, the provisions for connectivity between the receiver arrays and the mixers are presented.

2.2.1 Stage I: Design of the imaging system components

For an imaging system, the antenna design is critical and therefore is usually the first task to be undertaken. The main challenges in the design of a suitable antenna are the requirements for compact size, good impedance match in the frequency band from 3 GHz to 8 GHz, design complexity, and manufacturing cost. Here, the first step is the design of a single passive element (antenna), for a receiving array that can satisfy the above-mentioned requirements.

Once a satisfactory impedance performance is achieved for a single antenna element, the next step is to design the array. The first goal has been the design of a

3×3 element array in simulations. This array size is chosen to keep the computational time of the electromagnetic simulations acceptable. The simulations with the chosen array size take between 2 and 3 days, which is reasonable given the computational complexity. Array sizes larger than this lead to prohibitively long simulations times and thus are not suitable for the initial design stages.

The design of arrays mainly focuses on minimizing the mutual coupling between the neighboring elements. It is important to design and tune the antenna element in array configuration because the array is dense and special attention must be paid to the reduction of the inter-element coupling. The current distribution on each antenna element in the array is influenced by the adjacent antenna elements. This leads to changes in the input impedance and the radiation pattern of the individual antenna elements. The antenna coupling is detrimental to the image reconstruction as well since the signal received by the desired antenna element contains not only the signal it receives but also signal components due to the neighboring elements. This is why it is important to suppress the mutual coupling as much as possible while maintaining small inter-element spacing. Optimizing with these conflicting requirements is crucial in order to achieve acceptable performance.

The next task is the fabrication of the passive antenna array prototype and the measurement of the S-parameters in order to confirm the performance of the antenna array, both in terms of impedance matching and the mutual coupling among the elements. The first planar, passive antenna array prototype, operating from 3 GHz to 7.5 GHz, for the proposed system architecture is reported in [54]. Simulations were performed for a 3×3 antenna array, and an 11×11 element array was prototyped to validate the design performance. The fabricated antenna array is shown in Fig. 2.2. The design of [58] was adopted and modified for the antenna array reported in [54]. Therein, the inter-element spacing is 12 mm, both in x and y directions as opposed to 13.1 mm and 11 mm reported in [58]. The impedance match of this prototype, varied between -8.5 dB to -10 dB from 3 GHz to 5 GHz. The design presented in this thesis provides an improvement in the impedance match performance, and the

details are presented in Chapter 3.

(a) (b)

Fig. 2.2. Photos of the fabricated antenna array in [54], consisting of 121 (11×11) elements: (a) top view of the metallization layer with the slots, which face the tissue phantom; and (b) bottom view of the metallization layer with the forks and the ground pads. Nine of the central elements in a 3×3 configuration are soldered to SMPS connectors.

The prototyping and measurement of the passive array is followed by the integration of a low noise amplifier (LNA) chip with each element of the array. A careful layout design of the transmission lines is required to achieve low-reflection low-loss transition from the antenna to the LNA. To verify the performance of the on-chip LNA, this stage requires co-simulation of the design to incorporate the S-parameters of the chosen LNA and to verify the gain obtained in the required frequency range from 3 GHz to 8 GHz. The co-simulation verification is followed by the prototyping and measurement of the active antenna array. The first active sensor array for our envisioned system architecture is reported in [59]. There, the LNA is integrated directly with the antenna as shown in Fig. 2.3. The expected gain of 20 dB is observed in both simulations and measurements. The disadvantages of this design and the

respective design improvements are presented in this thesis in Chapter 3.

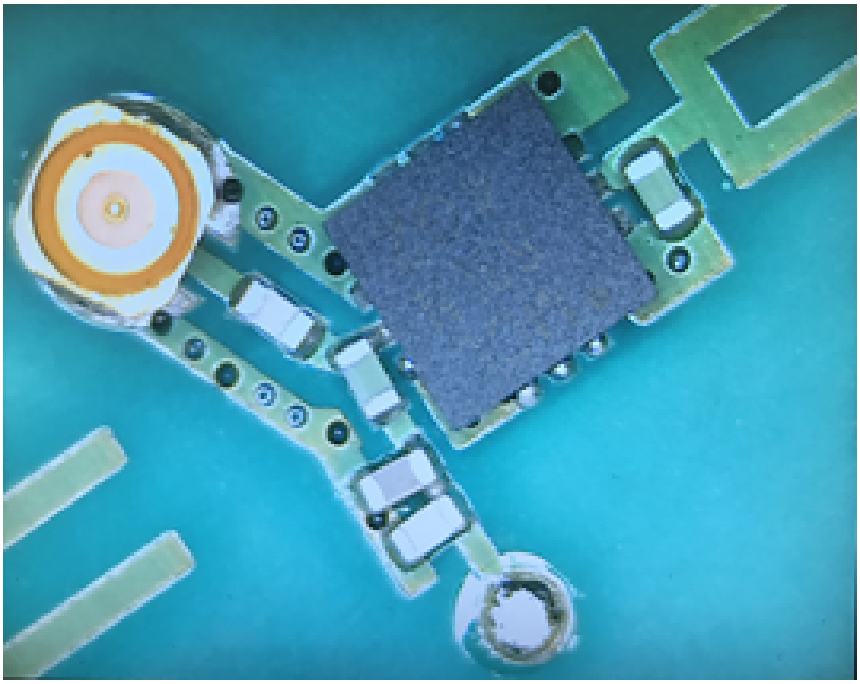

Fig. 2.3. The diagram shows the active antenna element [59], where an LNA chip is integrated directly with the antenna. The bias-tee components can also be observed here.

The transmitting array in the envisioned architecture can employ the same passive antenna element as the one used in the active receiving array. The challenge on the transmitting side is the development of a power splitting network that would provide power to hundreds of elements available in the array. Power dividers with a large number of outputs, as high as 32, are available off-the-shelf in the low-gigahertz frequency ranges. An example of a coaxial power divider that works in our desired frequency range is Mini-Circuit's ZC16PD-02183-S+ [60], which has 16 outputs and ranges from 2 GHz to 18 GHz with typical isolation of 33 dB between its channels. Multiplexing using these single pole sixteen throw (SP16T) switches provides the needed RF power supply to one or more transmitting antennas in any desired pattern. On the other hand, achieving a planar and compact RF power-splitting network remains a challenge that needs to be addressed in the future. Fabrication of the Tx array prototype and its measurements with the power divider network included must follow. For an antenna array to be successfully employed for transmission a smooth

field distribution is an important requisite. Also, it is desirable that maximum power is coupled into the tissue with minimum leakage into the air. The field distribution of the designed antenna array is discussed in Chapter 3.

The most challenging steps in the development of the envisioned imaging system are the design of the mixer array and its interconnect with the active antenna elements. In the first stage of this development, a passive mixer is considered for the down-conversion of the RF input to the IF output. There are two strategies regarding the design of the mixer array. The first strategy envisions the integration of both the LNA and the mixer at the antenna terminals on the same printed circuit board. In view of the very limited area available (12mm $\times$ 12mm), it would be very challenging to accommodate both an LNA and a mixer chip along with the DC bias traces, the LO and RF transmission lines, and the IF output traces. This challenge can be easily overcome if the LNA and the mixer are implemented on a single-chip platform. Unfortunately, such chips are not currently available in the UWB range from 3 GHz to 8 GHz. This is why our team is currently working on the design of such a UWB high-performance receiver on a chip. We also have to keep in mind that the ultimate goal of our architecture is to provide a wireless LO, although, in the first prototyping stage, we are considering a wired LO transmission. The second strategy envisions a mixer array that is completely separated from the antenna array i.e., it is implemented on a separate printed circuit board (PCB). In this case, providing the LO signal is easier along with a more straightforward layout of the hundreds of IF outputs. To connect the antenna array with the mixer array, a vertical high-speed connector [61] is being considered, as shown in Fig. 2.4. The details of this connector are discussed in Chapter 4.

For the completion of the imaging module, the design of the switching network for multiplexing a large number of IF outputs is necessary. As discussed in Section 2.1, the architecture employs two sets of switches: (a) IF switches which multiplex the IF output to the 50 Ohm port of the VNA, and (b) DC LNA-bias switches which will work synchronously with the IF switches. These switching networks are crucial

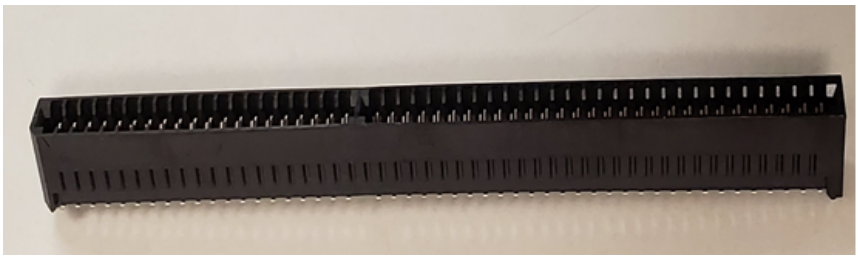

Fig. 2.4. Vertical high-speed connector from SAMTEC [61]. It is a 2 mm pitch, dual row connector with 50 contacts per row. It is a surface-mount connector that can accommodate a vertical PCB with a thickness of either 1.6 mm or 2.36 mm.

in improving the overall dynamic range of the system. To understand the importance of bias switching, let us consider an example. A typical RF switch provides isolation between 30 dB to 40 dB, depending on the frequency range and the manufacturer. A representative single-pole eight-throw (SP8T) RF switch from Analog Devices HMC321ALP4E [62] provides typical isolation that ranges from 50 dB (from DC to 2 GHz) to 30 dB (DC to 8 GHz).

This switch is only one of the many off-the-shelf choices that are suitable for the IF switching network that will operate at 10 MHz or 30 MHz, depending on the choice of the active mixer. The range of isolation between the output channels is insufficient to provide the desired 100-dB dynamic range. To overcome this deficiency, the IF switching is augmented by the bias-switching. The advantage of such a system has been reported in [63], where a dynamic range of 127 dB is reported based on simulated results. Therein, along with switching the bias of the LNA ON/OFF, the bias of an active mixer is also controlled. The difference in the signal output between the ON and OFF state of the channels is more than 100 dB. In other words, the outputs of the channels that are muted by OFF bias lie below the noise floor of the VNA, and hence the dynamic range of the system is limited only by the noise floor of the VNA.

2.2.2 Stage II: System integration

In the previous section, we advocated the use of a two-level (LNA DC bias and IF) switching system to improve the dynamic range of the imaging system. In the

first stage of its development, our prototype employs off-the-shelf LNA and passive-mixer chips. Here, we note that a system with passive mixers cannot provide a dynamic range as large as the one with active mixers. Unfortunately, the currently available off-the-shelf active mixers do not cover the required frequency range of 3 GHz to 8 GHz. To address this problem, we also focus on an in-house custom-design chip, which includes both the LNA and the active mixer for a conversion gain greater than 10 dB. In addition to maximizing the dynamic range and the channel isolation, this architecture will also allow for the integration of both devices directly at the antenna terminals and therefore, will further simplify the system interconnect design.

Another major task for stage two is to accommodate a wireless LO transmission. The advantages of a wired LO network are the strong signal and frequency independence. The wireless LO, on the other hand, can provide the reference signals, which are advantageous in image reconstruction. Acquiring reference background signals is a mandatory step in the calibration of the imaging system. Acquiring these signals through the LO network simultaneously with the measurement of the object under test eliminates the need to perform a separate background measurement through the RF channels thus saving system-calibration time. The wireless LO channel, however, has a disadvantage namely, small-signal, which is frequency-dependent. This will result in frequency-dependent gain of the mixer. A major design challenge will be to overcome this disadvantage.

The final step is the fabrication of the entire system prototype, including the in-house receiver chips integrated within the antenna array and the wireless LO antenna array.

Chapter 3

Antenna Array Design for Imaging of Breast

3.1 State-of-the-art

The advantages offered by microwave imaging over the existing breast imaging techniques attracted the attention of various research groups around the globe. This, in turn, provided momentum to the design and development of antennas, that could comply with several criteria to make them suitable for this application. The most important design specifications include impedance bandwidth, size, design complexity, and cost of manufacturing. The design of the antenna is also influenced by the surrounding environment. For example, if the antenna is immersed in a coupling medium to alleviate skin-air reflections, its design does not typically require electromagnetic (EM) shielding, but it does require a coating layer to protect the antenna from the immersion liquid. In contrast, antennas that come in direct contact with the skin and are not immersed in liquids, require full EM shielding (except the radiating aperture) but they do not need protective coating.

The medium in which the antenna operates is a decisive factor in its design. The breast tissue has significant loss and dispersion. At each frequency, the complex

wave number is calculated as

$$k = \omega \sqrt{\mu_0 \epsilon_0 (\epsilon_r' - j\epsilon_r'')} \tag{3.1}$$

where $\epsilon_r' - j\epsilon_r''$ is the complex permittivity. The attenuation is the function of permittivity (ϵ) and conductivity (σ) of the medium and also of the frequency (f) of operation. The expression for the attenuation constant is given as

$$\alpha = \omega\Big(\frac{\mu\epsilon'}{2}\Big[\sqrt{1 + \Big(\frac{\epsilon''}{\epsilon'}\Big)} - 1\Big]\Big)^{\frac{1}{2}}, (\text{Np/m}). \tag{3.2}$$

Here, $\epsilon' = \epsilon_r' \epsilon_0$, $\epsilon'' = \sigma/\omega$ and $\omega = 2\pi f$. The attenuation as a function of distance z is then defined as

$$|P(z)| = P_0 e^{-2\alpha z}. \tag{3.3}$$

The wavelength also changes as a result of the variation in propagation constant, given by the expression, $\lambda_{\text{eff}} = \lambda_0 / \sqrt{Re(k)}$, where λ_{eff} is the wavelength in the medium and λ_0 is the wavelength in free space. The antenna size is generally defined as a fraction of the wavelength. Moreover, the spatial resolution of the images requirement is limited by the wavelength and is given by the diffraction limit [40]

$$\Delta\zeta_{\max} \approx \frac{\lambda_{\min,\text{eff}}}{4 \sin\alpha}, \zeta \equiv x, y. \tag{3.4}$$

Here, $\lambda_{\min,\text{eff}}$ is the shortest wavelength of the radiation in the medium, and $\alpha_{\max}$ is the largest angle of arrival (i.e., viewing angle) at which the scattered signal can be received. This angle is determined either by half of the antenna beamwidth or half of the angle subtended by the aperture, whichever is less. In tissue, the effective angle α is small because increasing it implies longer signal paths, which in turn results in weaker signals. A trade-off between dense sampling and lower mutual coupling between array elements is necessary and is an important design challenge. From the above discussion it is observed that the size of the antenna depends on the medium of operation. In turn, the antenna size decides the spatial sampling or how dense the array could be packed.

A broad classification of the antenna design for microwave imaging can be done on the basis of the method being employed, which is either microwave tomography (MWT) or synthetic aperture radar (SAR). The basic difference in these techniques is the frequency range being utilized. Microwave tomography is a narrowband approach, where the antennas normally operate in the lower frequency range, sometimes as low as 300 MHz. A microwave imaging system operating at 2.45 GHz is reported in [64]. The system is composed of 64 antennas located on the perimeter of a cylindrical liquid filled chamber. Specially modified waveguides with an aperture of 30×9 mm^2 are used as antennas. Another system employing microwave tomography utilizes 16 transceiving monopole antennas operating in the frequency range from 300 MHz to 1000 MHz [55]. Monopole antennas have been chosen since they can be effectively modeled as a line source. This provides the best match between the numerical model and the practical imaging set-up. Additionally, they act as excellent radiators in a lossy environment, where resistive loading substantially increases the usable bandwidth [28]. Another prototype for MWT using a monopole antenna array is reported in [65]. It is a wideband system, operating from 1 GHz to 3 GHz. The eight-antenna configuration forms a circular ring inside an outer acrylic tank. Vertical and horizontal mounts allow to control the antenna positions with good precision and vary their height as well as the array diameter.To overcome the absence of a switch matrix, bi-static data is collected by switching manually the receiver to the available seven positions as one is fixed for the transmitter. Once the sweep of seven receiving position is completed, the transmitter position is switched.

The antenna elements used in radar-based imaging exploit an ultra-wide bandwidth. Various types of ridge-horn antennas have been developed for microwave breast imaging. In [66], a double-ridged horn antenna is designed to operate in the frequency range from 1 to 6 GHz. The performance of this antenna is compared to that of a Vivaldi antenna by measuring reflection from a breast phantoms. It is shown that the double-ridged horn provides a higher contrast in all reconstructed images. Similarly, in [67], a pyramidal horn antenna was designed with one ridge on the lower plate and the other ridge replaced by a curved metallic launching plane

on the upper plate. The curvature and shape of the plate are optimized to minimize reflections and provide good impedance matching with a coaxial feed. The designed antenna operates over the range of 1 GHz to 11 GHz. A dielectric medium is used in [68], to enclose a TEM horn antenna. This provides an impedance match for power delivery to the tissue when the antenna is pressed against it (see Fig. 3.1). Similarly, in [69], [70], a TEM horn was placed in a solid dielectric medium. Copper sheets are placed on the top, bottom, and sides of the antenna resulting in better radiation efficiency, blocked interference, improved coupling efficiency, and good impedance match. Small apertures are also introduced in the top sheet of the shield, providing a uniform field distribution.

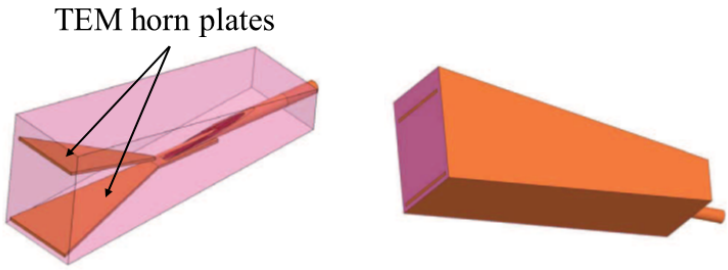

Fig. 3.1. The TEM horn antenna reported in [68]. The left picture shows the horn antenna inside the solid dielectric. The one on the right shows a shielded antenna element.

Due to their broadband behavior, Vivaldi antennas have been of interest for many years [71]. Adding corrugations to the conventional Vivaldi structure can help achieve a broader bandwidth and higher gain. In [72], the lengths of the corrugations in a Vivaldi antenna are optimized to reach a broad impedance bandwidth from 1.96 GHz to 8.61 GHz. Other variations, such as the balanced antipodal Vivaldi antenna (BAVA) [73], [74], or the double exponentially tapered slot antenna (DETSA) [75], have also been reported.

Monopole antennas have been widely used in microwave breast imaging research, as they can be modified to achieve wide bandwidth. A square monopole antenna presented in [76] offers a small size of 10×10 mm^2 while operating in the frequency range of 4 GHz to 9 GHz. The operational bandwidth of a monopole structure can

be significantly increased by performing some modifications to the ground plane to provide electromagnetic coupling between the radiating patch and the ground plane, without enlarging the size of the antenna. Such designs are reported in [77], [78] and [79].

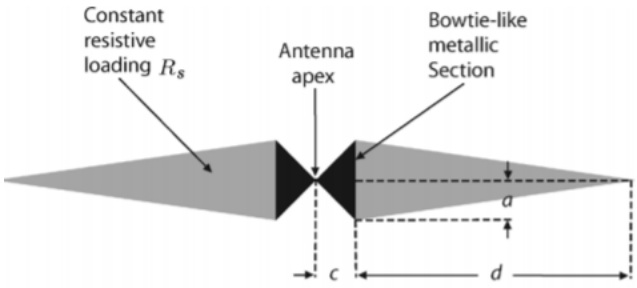

Fig. 3.2. The geometry of the resistively loaded "Dark Eyes" antenna. The dimensions are (in mm): $a = 5$, $c = 5$, and $d = 35$ [80].

Several bow-tie antenna configurations have also been investigated for breast imaging. A compact bow-tie antenna is reported in [81], where antennas of size 62.5×62.5 mm^2 are presented. To block waves propagating away from the breast, an octagonal cavity is placed behind the bow-tie elements and is attached using a metal flange. It has been observed that the broadband performance of the antennas can be improved by variable resistive loading. A bow-tie antenna with resistive loading is reported in [80]. The design is named "Dark Eyes", as the geometry resembles the shape of eyes as shown in Fig. 3.2. A sensor array with nine bow-tie antennas has been reported in [45]. Five elements are co-polarized, while the other four are cross-polarized (see Fig. 3.3). The bow-tie elements face the measured tissue phantom while the back of the PCB is glued to a solid dielectric medium. This region maximizes the coupling of power into the tissue phantom. Also, the surface of the dielectric cylinder is covered by copper sheets to minimize the ambient electromagnetic interference and to prevent power leakage away from the tissue.

Slot antennas are another common choice in microwave breast imaging as they conform to a number of design requirements such as ease of fabrication, compact size and wideband impedance match performance. A comparison of a stacked patch

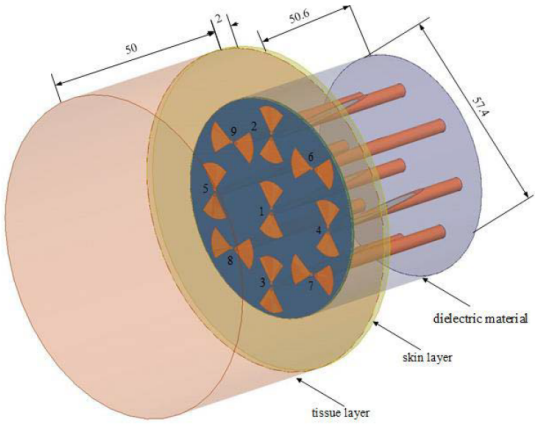

Fig. 3.3. Diagram showing nine bow-tie elements in co-polarized and cross-polarized configurations, a skin layer, and a tissue layer [45]. All dimensions are in mm.

antenna and a wide-slot antenna for breast imaging has been reported in [82]. The wide-slot antenna performed well over the entire angular/frequency range and faithfully radiated pulses at angles up to 60° away from bore-sight, whereas the stacked patch design exhibited significant late-time ringing and distortion of the transmitted signals. Also, the size of the slot design is significantly smaller than that of the patch antenna. Sugitani *et al.* proposed a 4×4 slot antenna array in [58], working in the frequency range from 3.5 GHz to 15 GHz. It has been shown that the system is able to detect a tumor of $10 \times 10 \times 1$ mm^3 size with a 10 mm separation distance. An 11×11 array of slot antennas is presented in [54]. Here, the antenna array is backed by a number of dielectric layers in order to improve the forward power coupling.

The following observations can be made from the above discussion. (a) Although the Vivaldi antenna designs provide a wide bandwidth, they suffer from large sizes, making them unattractive for array systems. On the other hand, the antipodal Vivaldi antenna designs offer a smaller size compared to the other Vivaldi antennas while exhibiting a broadband behavior. (b) Monopole antennas perform well within limited bands of the UWB range by modifying their ground planes. (c) Ridge and TEM horn antennas offer wide bandwidth, but they suffer from large size and a higher manufacturing cost compared to the microstrip antennas or slot antennas, making them unattractive choices for microwave imaging array systems. (d) Slot antenna

designs are a promising choice for microwave imaging, due to their planar and compact design. Moreover, a wide-band performance with good impedance match can be achieved.

3.2 Drawbacks of the existing antenna prototypes for the proposed system architecture

The designs reported in [54] and [59] provide important advantages, for example, they operate in direct contact with the human body and do not require coupling liquids, can be fabricated on a PCB, and provide back shielding that reduces interference and directs most of the energy in the forward direction into the tissue. However, the reported passive and active array prototypes suffer from two drawbacks. One drawback of the passive antenna array [54] is its input impedance performance. The reflection coefficients, both simulated and measured, see Fig. 3.4a, are as high as -8.5 dB, below 5 GHz (for a single element). This performance can be improved for an impedance match better than -10 dB, and it also needs to be ensured in an array setting, where the input impedance of each element is affected by its neighboring elements due to mutual coupling. The design presented in this thesis improves this performance (achieving a reflection coefficient below -10 dB) of each element individually, as well as in an array setting for the frequency range from 3 GHz to 8 GHz.

The second drawback of the existing active array design [59] can be understood by inspecting Fig. 3.4b. We see that in order to expose the area where the LNA and the connectors are placed (same level as that of the antenna feed, below the backing layers), holes are dug manually. This is completely impractical in a large array of 18×18 antenna elements. Thus, this structure poses serious limitations in terms of manufacturing.

To mitigate the two shortcomings of our existing prototype, a new design is proposed, which provides complete isolation of the electronic components from the

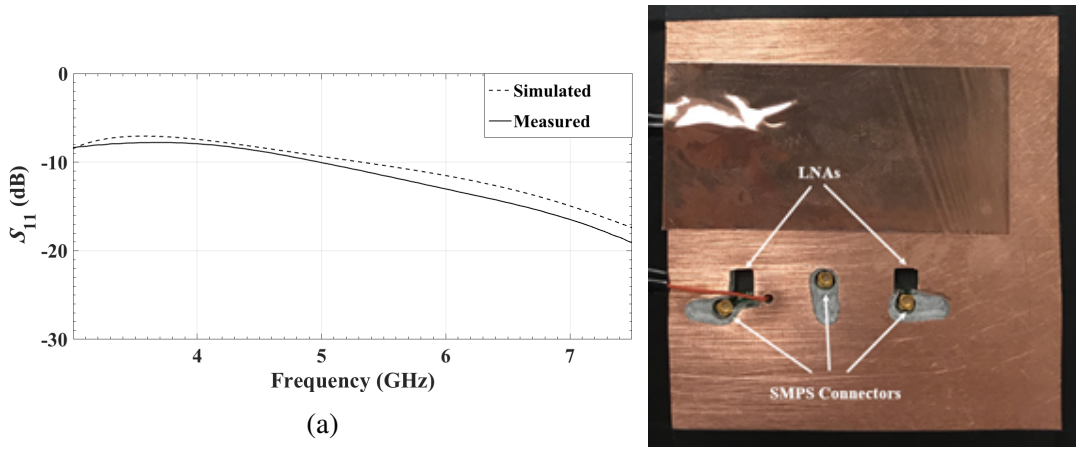

(a) (b)

Fig. 3.4. (a) The simulated and the measured reflection coefficients of a single passive antenna element reported in [54], and (b) the image showing the back side of the active array reported in [59]. It can be observed that in order to place an LNA and to access the output connectors, the backing layers have been manually scraped.

antenna. This is achieved by placing all the electronic components to the top layer above the shielding layer. The following design goals are defined for the antenna array presented here: (a) the reflection coefficients of the antenna elements must be below -10 dB for the frequency range from 3 GHz to 8 GHz; (b) the mutual coupling between the array elements must be below -20 dB; and (c) the electronic components, such as low-noise amplifier chips and connectors, must be located at the top metallization layer of the PCB for easy access and they must be isolated from the antenna elements by a shielding metallization layer between the antenna layer and the electronics layer. The next section discusses the multi-layer stack-up of the new proposed design along with the configuration of a single passive antenna element.

3.3 Proposed antenna array: design and development

This thesis proposes a planar array of ultra-wide band (UWB) active slot antennas for applications in the microwave imaging of the breast. The frequency band being employed is from 3 GHz to 8 GHz. The center-to-center element spacing is 12 mm, both in x and y directions. A low-noise amplifier (LNA) is integrated with

each antenna element for use in a receiving configuration. The proposed structure resolves the outstanding problem in the design of large active antenna arrays for tissue imaging, namely, the isolation of the antennas from the electronic circuits. A ground plane within the multi-layer design separates the antenna array from the electronics array while providing shielding to the antennas from the back and improved power coupling into the tissue. The critical development lies in the design of a low-reflection triple-wire vertical transition that carries the signal from the antenna layer to the electronics layer, where the LNA array resides. The vertical transition at each antenna element traverses through the stack-up of multiple layers of different permittivities and through openings in the shielding ground plane.

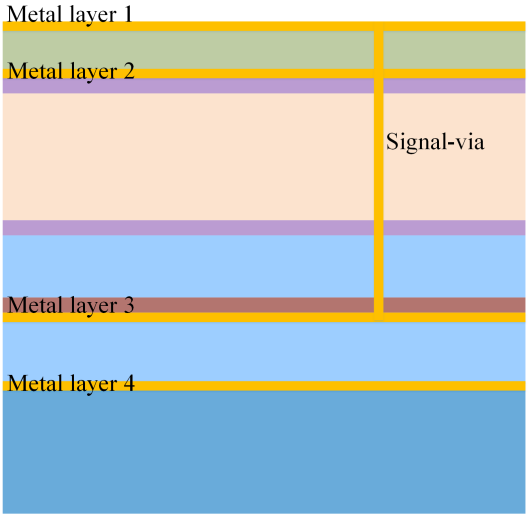

(a)

Materials	Thickness (mm)
Rogers 3035 (ε_r 3.5)	0.25
FR4 (ε_r 4.34)	2.5
Rogers RT/Duroid 6010LM (ε_r 10.2)	0.635
Copper	1 oz
Fastrise(ε_r 6.15)	0.14
Fastrise(ε_r 2.74)	0.14
Tissue layer	Semi-infinite

(b)

Fig. 3.5. (a) Multi-layer stack-up of the materials used in the simulations to investigate the performance of the antenna elements, and (b) color coded table showing the thickness, in mm, of the different materials being used in the stack-up.

3.3.1 Passive array configuration

The multi-layer stack-up and color coded table, depicting the material permittivities and their respective thickness are shown in Fig. 3.5. The permittivities, ranging from ϵ_r of 10.2 and loss tangent, tan δ, of 0.5 for the tissue, to ϵ_r of 3.5 and loss tangent, tan δ, of 0.003 for the top layer, where the electronic components are present. The vertical signal transition carries the signal through these different layers and

therefore is a major challenge, requiring careful design and optimization. A 3×3

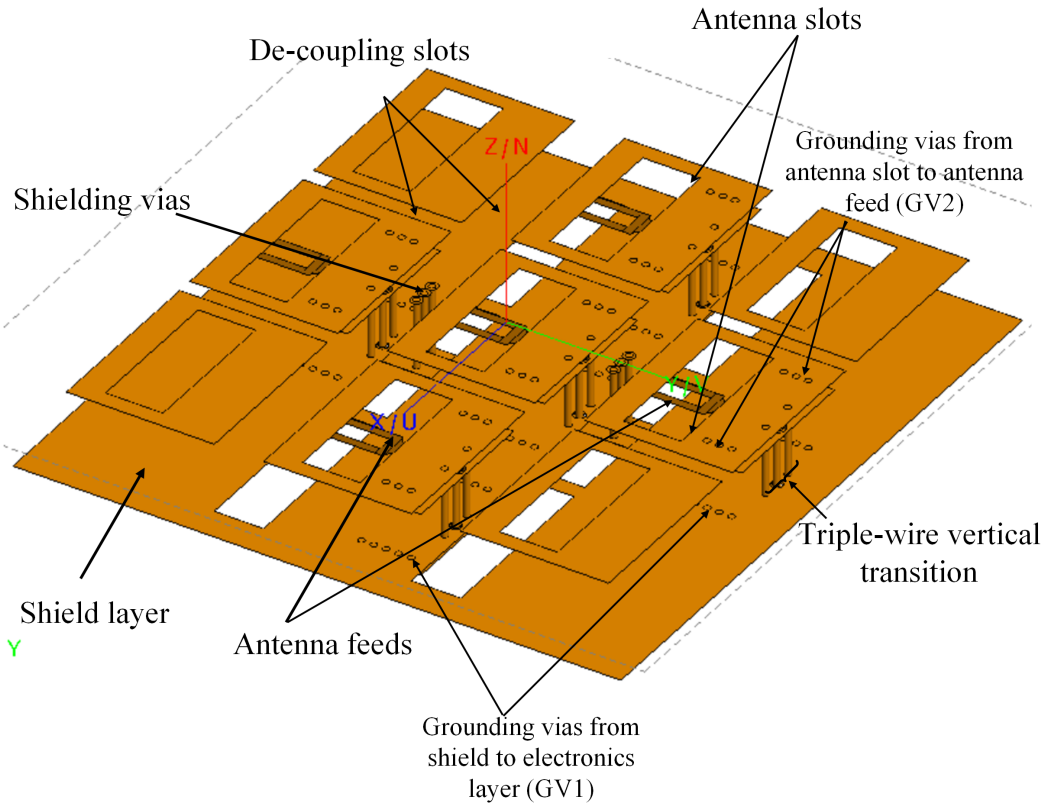

Fig. 3.6. The isometric view of the simulated 3×3 array (9 slot antennas).

antenna array with 9 antenna slots (see Fig. 3.6) has been simulated in FEKO to investigate the performance of the antenna elements in an array configuration. The diagram shows the simulated 9-element configuration with the mentioned stack-up. One center element, along with its four neighboring elements in a star configuration, is excited using an edge port at the electronics layer (not visible in Fig. 3.6, due to shield layer). Three metallization layers, namely, the antenna-slot layer (metal layer 4), the antenna-feed layer (metal layer 3), and the shield layer (metal layer 2) can be observed in the diagram. The complexity of the structure can be appreciated from the plot. The triple-wire vertical transition, novel in this design, can also be seen in Fig. 3.6. A number of vias are employed for proper grounding and shielding of the structure. The dimensions of these vias and their sizes are given in Table 3.1. A detailed description of each layer is presented next.

Table 3.1. Configuration of the different via-holes present in the passive array design

Name of the via-hole (Fig. 3.6)	**Size(ø)**	**Layers connected**
Signal via	0.4 mm	Layer 1 to Layer 3
Shielding vias	0.4 mm	Layer 2 to Layer 4
Grounding vias		
GV1	0.4 mm	Layer 1 to Layer 2
GV2	0.4 mm	Layer 3 to Layer 4

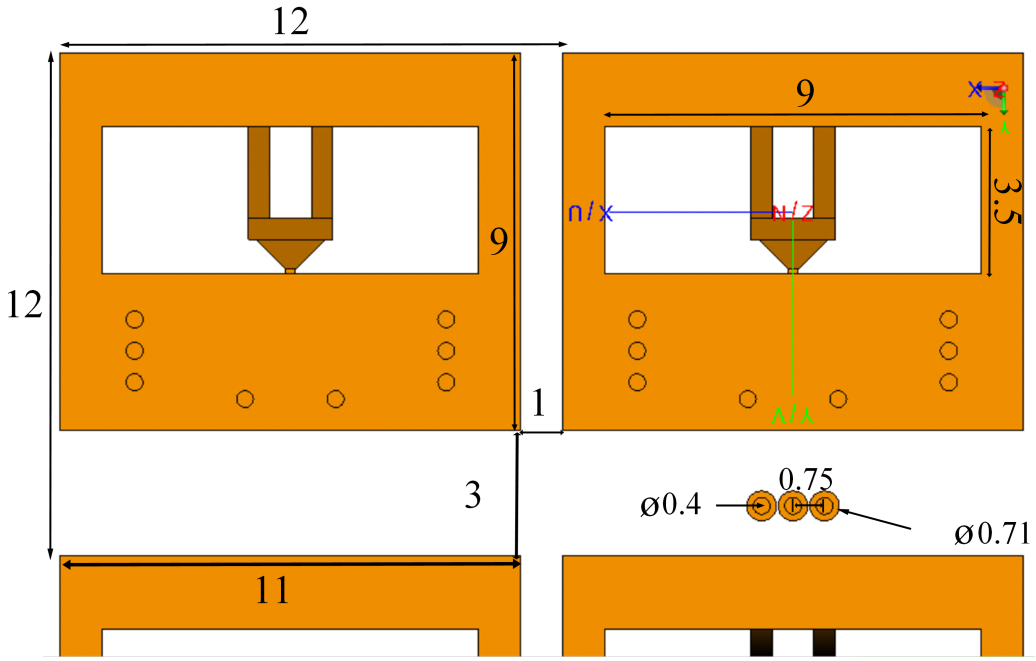

Fig. 3.7. The diagram shows the top view of a segment of antenna slot layer. Decoupling slots and shielding vias with dimensions (in mm) are shown.

The passive antenna structure resides on two metallization layers of a 0.635 mm thick Rogers RT/Duroid 6010LM substrate with dielectric constant ϵ_r = 10.2 and tan δ = 0.002. The antenna slot resides on metal layer 4 whereas the antenna feed is at metal layer 3. The slot is electromagnetically fed by a fork. Both the slot and the antenna feed have been modified from the previous design of [54] to improve the impedance match. A segment of the antenna slot layer is shown in Fig. 3.7. The slot size is 9×3.5 mm^2. The center-to-center distance between the antenna elements is 12 mm, both in x and y directions, as shown in Fig. 3.7.

One of the challenges in the design of arrays is to minimize the mutual coupling among the elements. To suppress the coupling, decoupling slots are introduced to separate the antenna elements in the y direction (see Fig. 3.6). The size of these decoupling slots is 3×11 mm^2. The slots separating the antennas in the x direction are of size 9×1 mm^2 and they have been first proposed in [54]. They, too, serve to decouple the antennas. The slots result in the formation of what can be called "antenna islands".

The decoupling slots described above reduce the current from one antenna to the next.However, they are not sufficient to obtain coupling below -20 dB. As a next step, shielding vias are introduced to separate the elements in the y direction (see Fig. 3.7). These vias extend from the shielding layer (metal layer 2) to the antenna slot layer (metal layer 4). It can be observed that the position of these vias is carefully chosen to block the field from the slot, which is the strongest in the middle of the slot (sinusoidal distribution) and is polarized along the y axis. At the slot edges in the y direction, the electric field is zero, and therefore the neighbors in the x direction are weakly coupled in comparison to the ones in y direction. The design and dimensions

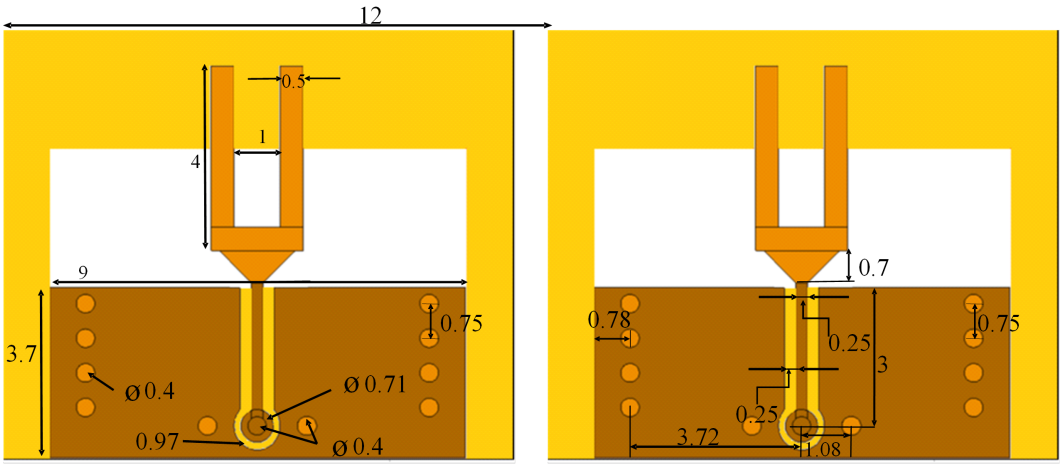

Fig. 3.8. The diagram shows the design and dimensions at the antenna feed layer. The antenna slot plane is shown in yellow, whereas the antenna feed (fork) with CPW transmission is shown in brown. Four grounding vias on either side of the CPW can also be seen. In addition, the top view of the triple-wire transition is also visible. All dimensions are in mm.

of the antenna feed are shown in Fig. 3.8. The signal captured by the antenna slot is

intercepted by the fork. The signal trace from the fork is then gradually transitioned into a co-planar waveguide (CPW) (see Fig. 3.8 for dimensions). This CPW, in turn, transfers the signal to the triple-wire vertical transition that carries the signal upwards to the electronics layer. At the electronics layer, another CPW takes the signal to the output terminals. In transmitting mode, the CPW at the electronics layer is fed using an edge-port (in FEKO simulations), as shown in Fig. 3.9.

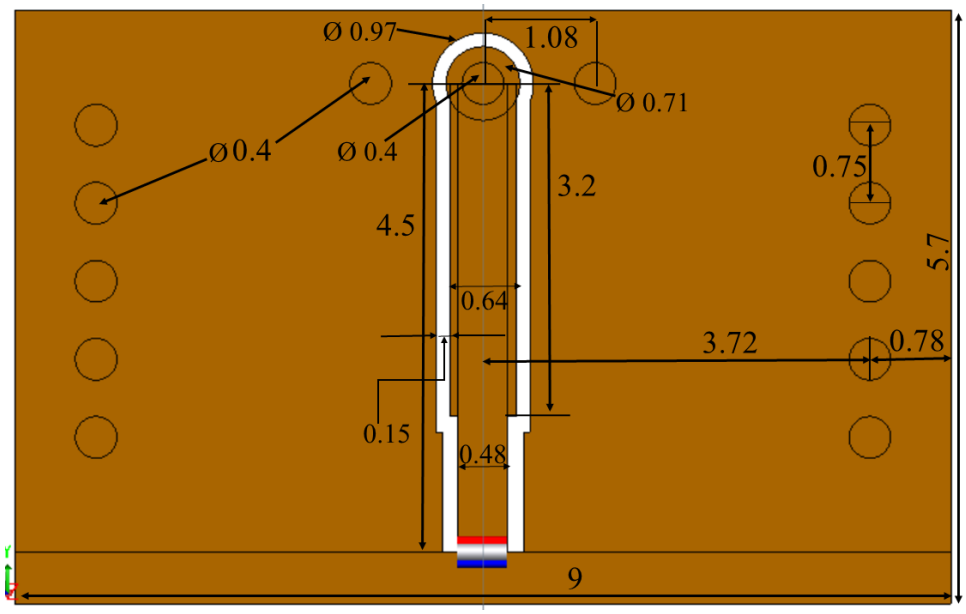

Fig. 3.9. The diagram shows the design and dimensions of the CPW at the electronics layer. The edge-port used for exciting the antenna in the FEKO simulations is also shown. The small capacitive intrusions to counter the inductive parasitics can be observed on either side of the signal line. All dimensions are in mm.

As mentioned earlier, the triple-wire vertical transition travels through a number of layers with varying permittivities and, therefore its design required a lot of optimization in terms of size in order to achieve a good impedance match. Furthermore, the height of the signal via is 3.805 mm, which is comparable to the antenna-slot itself. The long via introduces a parasitic inductance in the structure, which affects the input impedance of the antenna. To counteract these parasitics, capacitive intrusions are appended to the CPW (see Fig. 3.9), at the electronics layer. Both the length and the width of these intrusions are carefully chosen to comply with the manufacturing tolerance. In addition, a significant effort has been involved in optimizing the size

of the capacitive intrusions to achieve a good impedance match.

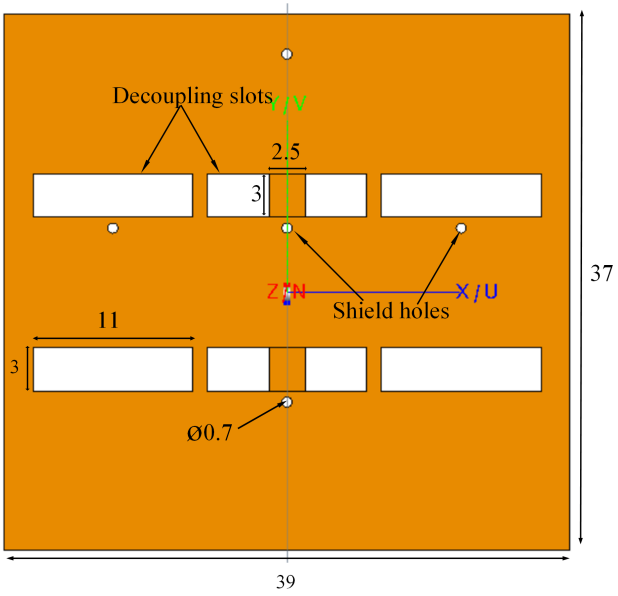

Fig. 3.10. The plot shows the shield layer of the antenna array. The shield holes allow the signal-via to pass. Also the mirrored decoupling slots can be seen. All dimensions are in mm.

An important feature of this array design is the shield layer that isolates the antenna from the electronics layer. The shield is shown in Fig. 3.10. We can observe the circular slots (shield holes) that allow the signal via of the triple-wire transition to pass through this layer towards the electronics layer. The decoupling slots at the antenna slot layer are mirrored at this layer. To accommodate the shielding vias, a small rectangular patch with dimensions 2.5×3 mm^2, is added to the decoupling slot.

A passive antenna array of 6×6 elements has been fabricated and is shown in Fig. 3.11. The measured performance of the prototype is discussed in the next section.

3.3.2 Active antenna element: design and simulation

The notion of integrating radio-frequency (RF) active electronics within the antenna is well-known and has been used in various fields such as microwave tissue imaging [59, 83, 84], medical radio-thermometers at 1.5 GHz [85], and ultra-wide

(a) (b)

Fig. 3.11. (a) The picture shows the electronics layer, with sub-miniature push-on sub-micro (SMPS) connectors in a star configuration. The SMPS connectors are also soldered to the edge elements, in order to investigate the performance at the end of the antenna board. (b) The antenna slot layer, of the fabricated 6×6 antenna array prototype.

band (UWB) multiple-input multiple-output (MIMO) systems [86], to name a few. It has been recognized that the integration of an LNA with the antenna can significantly improve the SNR of the system, which is one of the greatest challenges in microwave tissue imaging. This is why the development of an active, i.e., LNA integrated, antenna for tissue imaging arrays is critically important. In addition to improved SNR, such antennas offer system size reduction since the LNA becomes part of the antenna element with no or very little increase in its size.

In this thesis, an active antenna element has been designed and simulated using *Keysight Advanced Design System (ADS)* [87]. The layout of the design is shown in Fig. 3.12. This circuit includes all the components of the original LNA evaluation board, including the bias-tee. The footprint of the LNA chip (Mini-Circuits PMA3-83LN+) and the bias-tee components (C1, C2, C3, L1, and L2) are all as suggested in [88]. In receiving configuration, the scattered signal from the object under test (breast in this case), is captured by the slot antenna. The vertically transferred signal

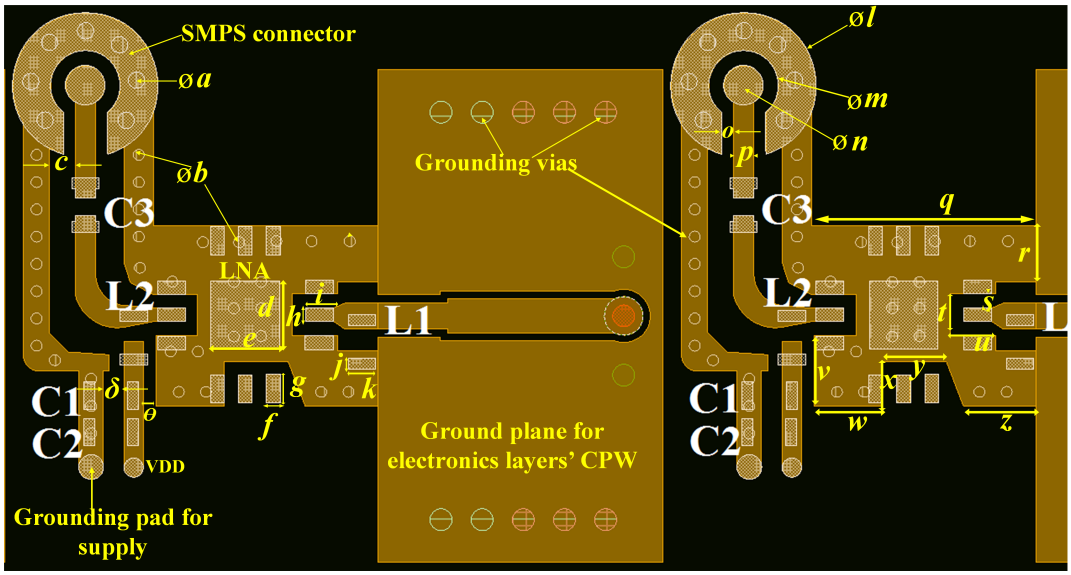

Fig. 3.12. The layout of the electronics layer of an active antenna element simulated in ADS (dimensions in mm). The diagram shows the footprint of the LNA with its biasing circuit components. The output of the CPW is connected to the input of the LNA. On the other hand, the LNA output is taken to the SMPS connector where the output is accessed in measurements.

is then amplified by the LNA. Here, the amplified signal is accessed using an SMPS connector [89]. The DC power for biasing the LNA chip is provided through the VDD pad and the ground pads. The dimensions of the layout are given in Table 3.2.

3.4 Simulated and measured results

3.4.1 Passive antenna array *S*-parameter results

To investigate the input-impedance performance of the passive elements, out of nine slot antennas in the 3×3 simulated array, five elements are connected to ports in a star configuration. The elements are fed using edge-ports (in FEKO) that are applied at the electronics layer as shown in Fig. 3.13. To obtain the reflection coefficient S_{11}, and the mutual coupling S-parameters (S_{21}, S_{31} etc.,) among the elements, the center element marked as Port 1 is excited. The four neighboring elements, marked as Port 2 to Port 5, are loaded with 50 Ohms.

Table 3.2. Dimensions at the electronics layer in the active array configuration.

Symbol	**Size**	**Symbol**	**Size**
a	0.300 mm	o	0.215 mm
b	0.254 mm	p	0.380 mm
c	0.510 mm	q	4.091 mm
d	1.250 mm	r	1.026 mm
e	1.250 mm	s	0.259 mm
f	0.251 mm	t	1.263 mm
g	0.517 mm	u	0.817 mm
h	0.249 mm	v	1.286 mm
i	0.511 mm	w	1.233 mm
j	0.200 mm	x	0.812 mm
k	0.500 mm	y	1.174 mm
l	2.640 mm	z	1.323 mm
m	1.270 mm	δ	0.379 mm
n	0.710 mm	θ	0.229 mm

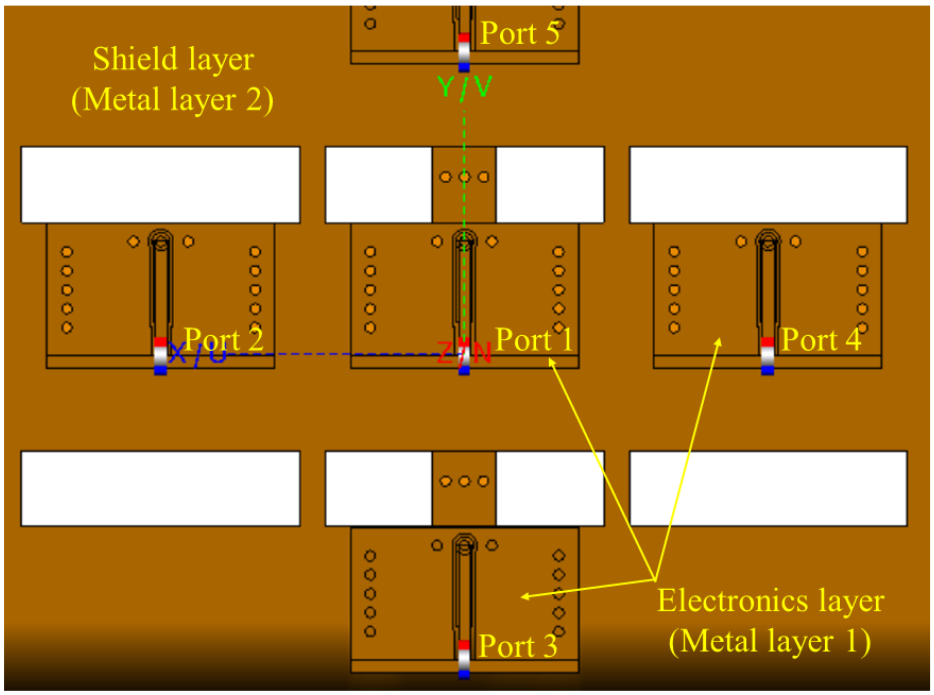

Fig. 3.13. The diagram shows the excited ports at the electronics layer of the passive antenna array elements in FEKO.

The measurement set-up of the star configuration is shown in Fig. 3.14. The antenna board is placed on 4 cm thick stack of carbon-rubber sheets (square sheets), that mimic the breast tissue. The center element of the configuration is connected to

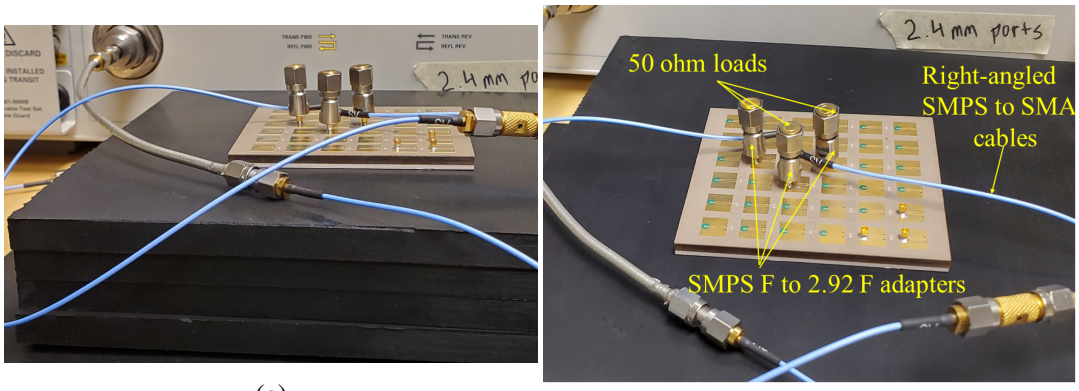

(a) (b)

Fig. 3.14. The photos show: (a) the side view of the *S*-parameter measurement set-up, where the antenna board is placed on 4 cm thick stack of carbon-rubber tissue phantom sheets and, (b) the top view of the same set-up. The center element is connected to Port 1 of the VNA, while one of the neighboring element is connected to Port 2. The three remaining elements of the star configuration are loaded with 50 Ohms SMA loads using SMPS F to 2.92 F adapters [90].

Port 1 of the Keysight (formerly Agilent) Technologies network analyzer (E8363B), while one of the neighboring element is connected to Port 2 of the network analyzer, using right-angled SMPS F to SMA cables (blue ones in Fig. 3.14) [91]. The rest of the elements are loaded with 50 Ohms SMA loads using SMPS F to 2.92 F adapters [90].

The comparison between the simulated and measured reflection coefficients S_{11}, is shown in Fig. 3.15. It can be observed that the simulated S_{11} lies below -10 dB for the whole frequency band from 3 GHz to 8 GHz whereas the measured S_{11} grazes the -10 dB threshold at the center frequencies. However, a similar trend can be observed in both curves.

Another goal for the design proposed in this thesis, is to achieve a mutual coupling below -20 dB among the antenna elements. The coupling *S*-parameters between the center element and its neighboring elements are plotted, in Fig. 3.16 to Fig. 3.19. We observe that both the simulated and the measured results satisfy the design requirement, but they are not in agreement with each other.

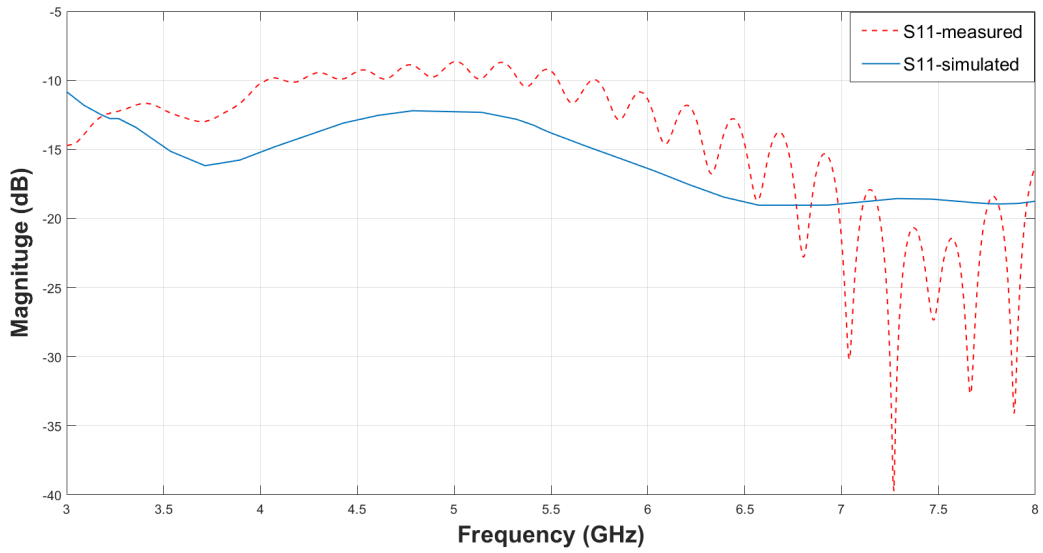

Fig. 3.15. Simulated and measured $|S_{11}|$, of the center element in the star configuration.

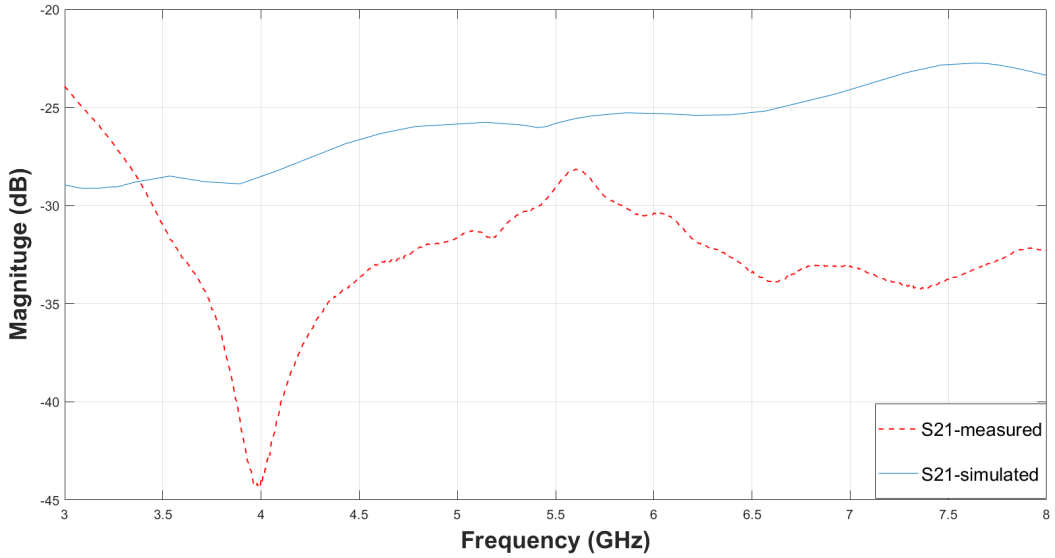

Fig. 3.16. Simulated and measured mutual coupling between the center element and the element at Port 2 in Fig. 3.13.

The discrepancies in the simulation and measurement results can be attributed to the following factors:

1. In simulations, the excitation is provided using an edge port (in FEKO) whereas the actual prototype is excited through an SMPS coaxial connector. The simulation

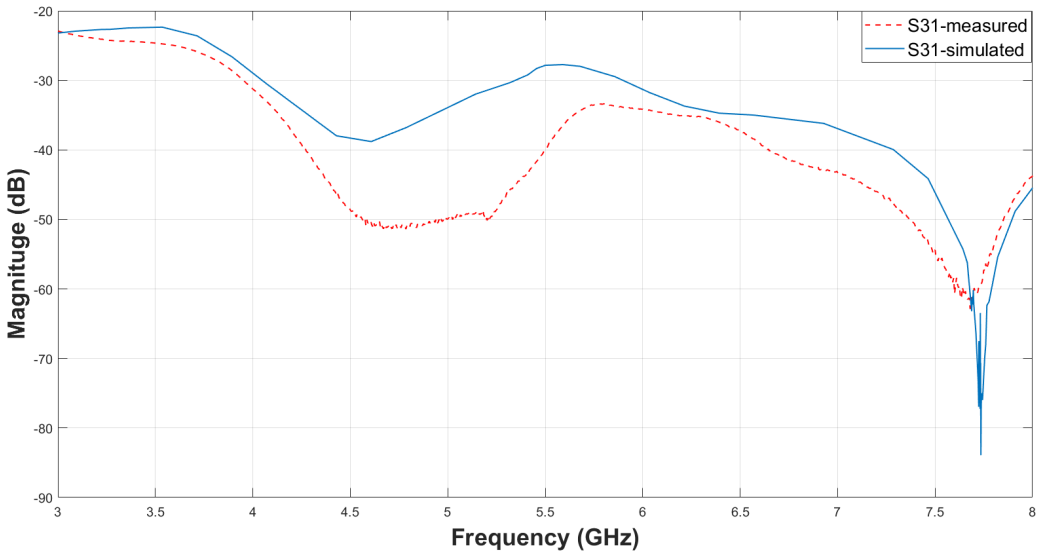

Fig. 3.17. Simulated and measured mutual coupling between the center element and the element at Port 3 in Fig. 3.13.

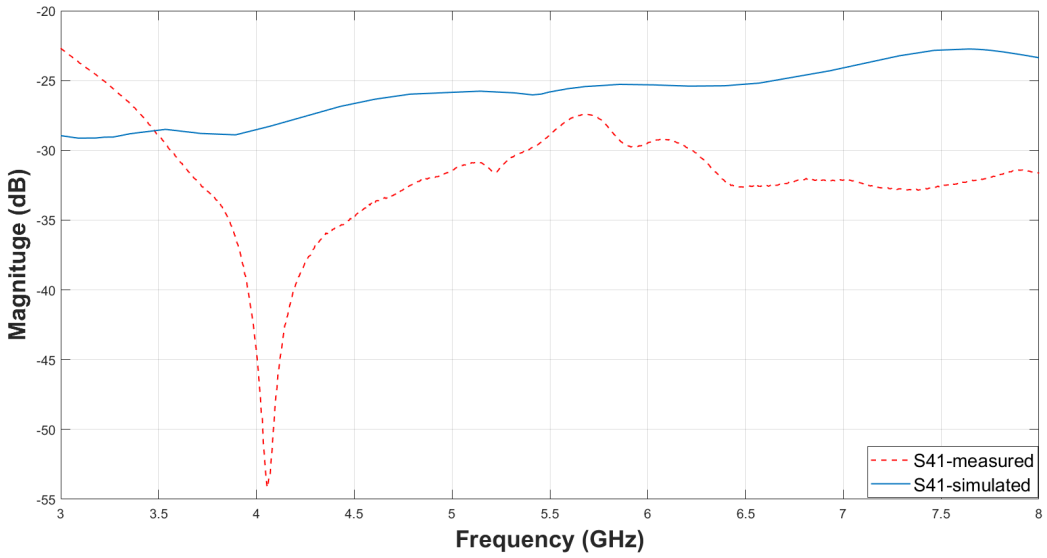

Fig. 3.18. Simulated and measured mutual coupling between the center element and the element at Port 4 in Fig. 3.13.

of an SMPS connector at each antenna element, even in the 3×3 array, results in a substantial increase in the computational time. This is a major difference leading to the deviations between the simulated and measured results as the input impedance is impacted by the port model.

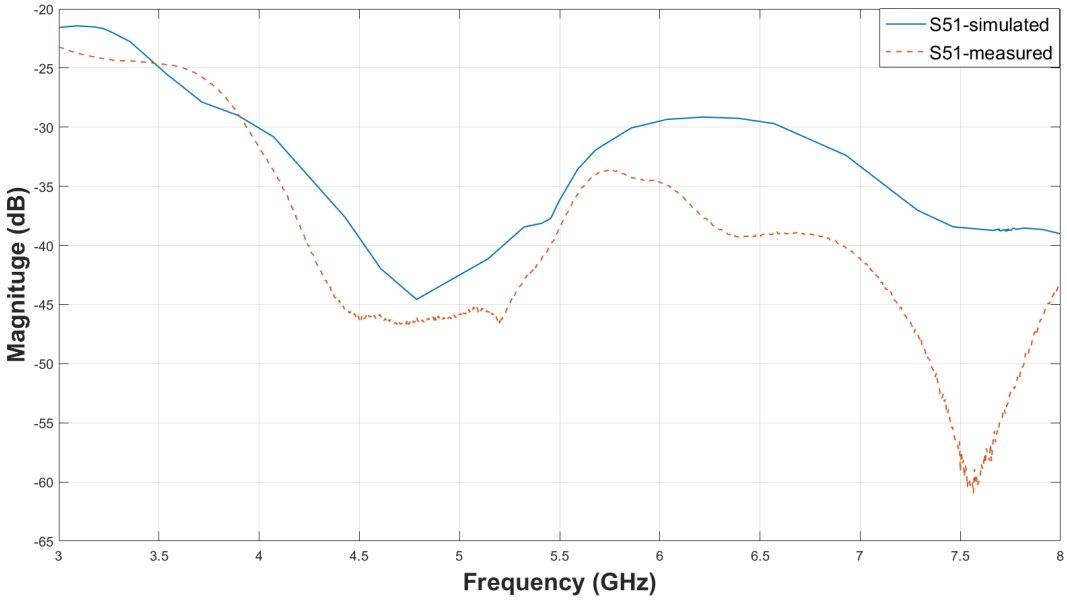

Fig. 3.19. Simulated and measured mutual coupling between the center element and the element at Port 5 in Fig. 3.13.

2. There is also a difference between the tissue medium defined in FEKO and the actual tissue phantom used in the experiments. In the simulation, the tissue layer is defined as a lossy dielectric layer. The constitutive parameters of this layer are ϵ_r of 10.2 and tan δ of 0.5, and these are constant over the bandwidth from 3 GHz to 8 GHz. On the other hand, the permittivity of the carbon–rubber tissue phantom used in measurements is frequency-dependent and is as shown in Fig. 3.20. It is to be noted here that the permittivity shown in Fig. 3.20 is lower than the value of these phantoms ($\epsilon_r = 10.2$, tan $\delta = 0.3$) measured more than 4 years ago. This change can be attributed to material aging.

3. Finally, the layer extents are also different. In the simulations the substrates and the tissue layer are infinite in the x and y directions. In the measurements, the tissue phantoms and the PCB layers are finite in the x and y directions. The lateral size of the square tissue phantoms is 20×20 cm^2 wheras that of the PCB is 7.7×7.8 cm^2

4. Another possible reason for the observed differences is the right angle bend in the SMPS to SMA cables [91] as well as the cables themselves since these cannot

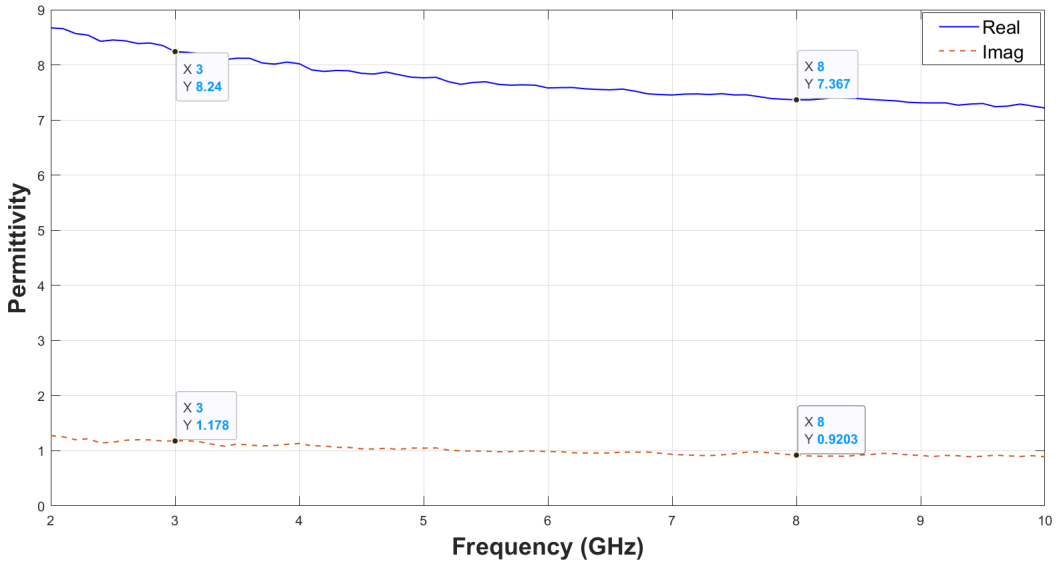

Fig. 3.20. The measured permittivity of the square carbon-rubber tissue phantom of thickness 1 cm. The permittivity of these phantoms is lower than the permittivity used in simulations. Also, they are frequency-dependent unlike the constant value used in simulations for the entire band from 3 GHz to 8 GHz.

be de-embedded using electronic calibration kit (Agilent N4692-60003, 10 MHz-40 GHz) .

3.4.1.1 Effects of different carbon-rubber phantoms on reflection coefficient measurements

In the previous section, we observed the discrepancies in the simulation and measurement results and one reason was the differences in the permittivities. Fig. 3.20 shows the permittivty of the square-shaped carbon-rubber tissue phantoms available in our lab. Another category of tissue phantoms, circular in shape, with higher permittivity and thickness (1.1 cm) than the square tissue phantoms, is also investigated to observe the performance of the fabricated prototype. The measured permittivity of the circular phantoms is shown in Fig. 3.21.

The *S*-parameter measurements are repeated with the set-up shown in Fig. 3.14 with square tissue phantoms replaced with the circular ones. It should also be noticed that the phantom thickness in this measurement is 4.4 cm as compared to 4 cm in

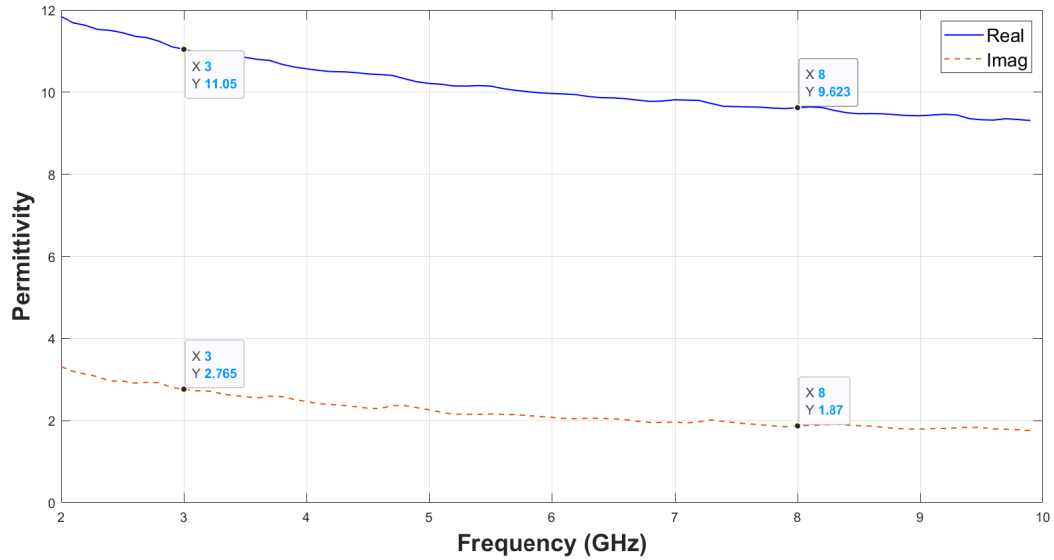

Fig. 3.21. Measured permittivity of the circular carbon-rubber tissue phantom sheets with a thickness of 1.1 cm. The permittivity is higher than that of the square tissue phantoms. It can be noted that these permittivity values are closer to the values in the simulations.

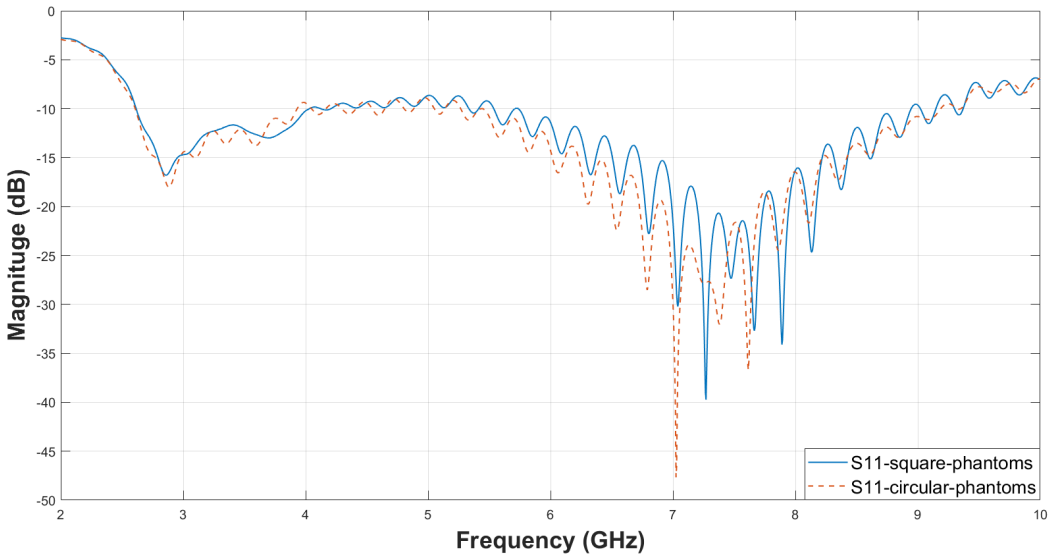

Fig. 3.22. Measured reflection coefficients of the center element of the star configuration with different tissue phantoms. The measurement set-up is the same as the one shown in Fig. 3.14.

the case of square phantoms. The obtained reflection coefficients in both cases are compared in the plot given in Fig. 3.22. Although the plots follow a similar pattern, differences can also be observed. It is interesting to note that the prototype provides

good repeatability of the measurements, with minor differences, when used with different tissue phantoms.

3.4.1.2 Effects on the input impedance of the center element with open and loaded neighboring elements

It is evident from Fig. 3.16 to Fig. 3.19 that the array design provides good isolation between its elements. Previously, the reflection coefficient of the center element has been measured while all the neighboring elements are loaded with 50 Ohms. To further investigate the performance of the prototype, the measurements on the center element are repeated. However, all the neighboring elements are now left open. The set-up is shown in Fig. 3.23.

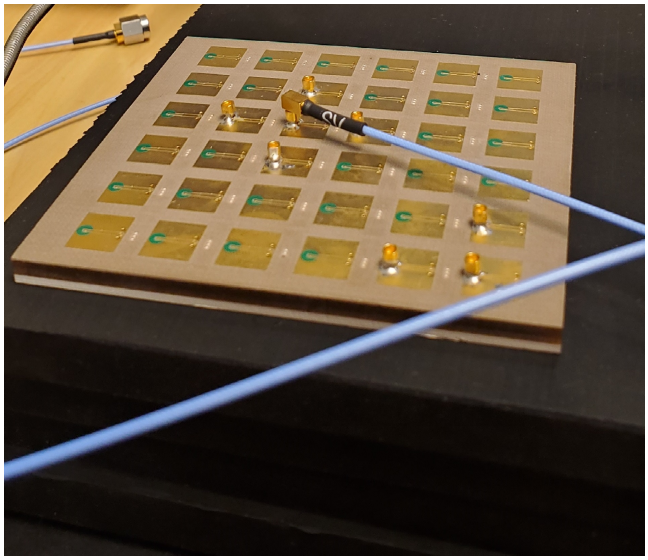

Fig. 3.23. Photo of the measurement set-up for the reflection coefficient of the center element of the star configuration with all the other elements open.

The plot in Fig. 3.24 shows the expected results. There are noticeable differences between the two curves, nonetheless, these differences are minor. This result is a reconfirmation of the good isolation among the antenna elements.

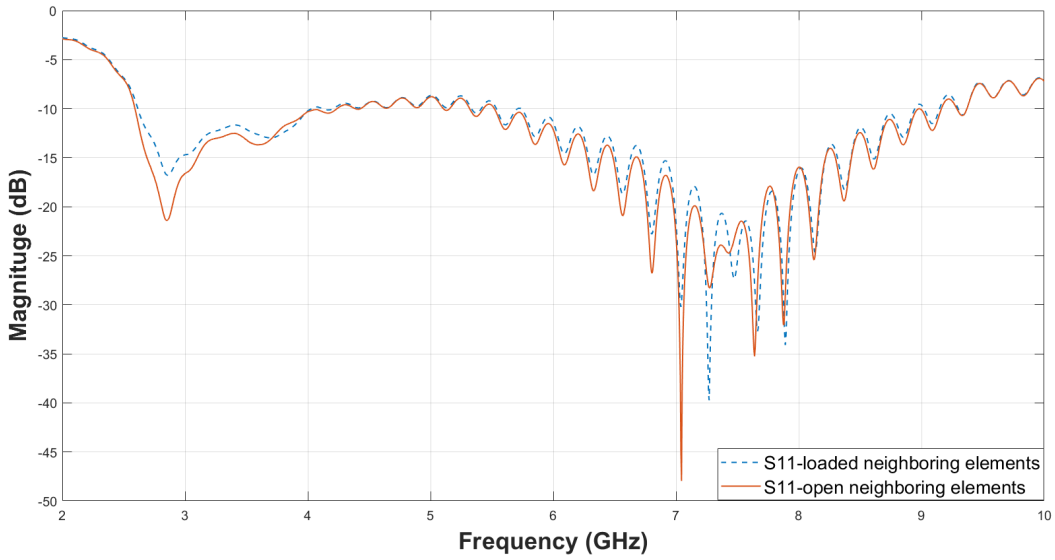

Fig. 3.24. The plot shows the reflection coefficients of the center element of the star configuration. In one measurement the neighboring elements are loaded with 50 Ohms and in the other, they are left open.

3.4.1.3 Field distribution of the center array element

Until now we have discussed the input impedance and coupling characteristics of the array design. Another important performance parameter is the near-field distribution of the antenna array. This array comes in direct contact with the tissue and therefore far-field radiation characteristics are not relevant.

As discussed before, the breast tissues are lossy and the signals beyond 6 cm from the skin-tissue interface suffer high attenuation. The distances smaller than this are part of the reactive near-field and Fresnel region of the antenna array. The normalized E-field distributions of the center element at 3 GHz, 5.5 GHz, and 8 GHz are shown in Fig 3.25. The field is plotted at a distance of 2 cm, 3 cm and 4 cm from the array into the tissue. A smooth field distribution can be observed. This provides an assurance that the passive array can be safely employed as a transmitting array with good radiation characteristics.

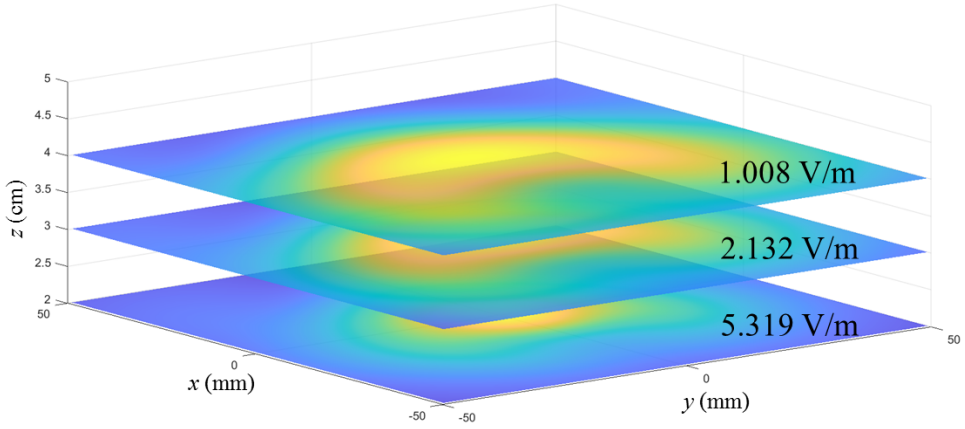

(a) Field distribution at 3 GHz

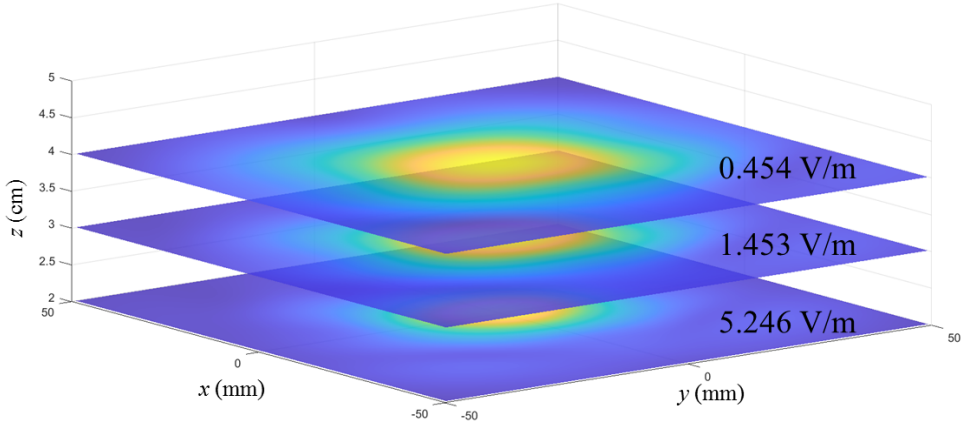

(b) Field distribution at 5.5 GHz

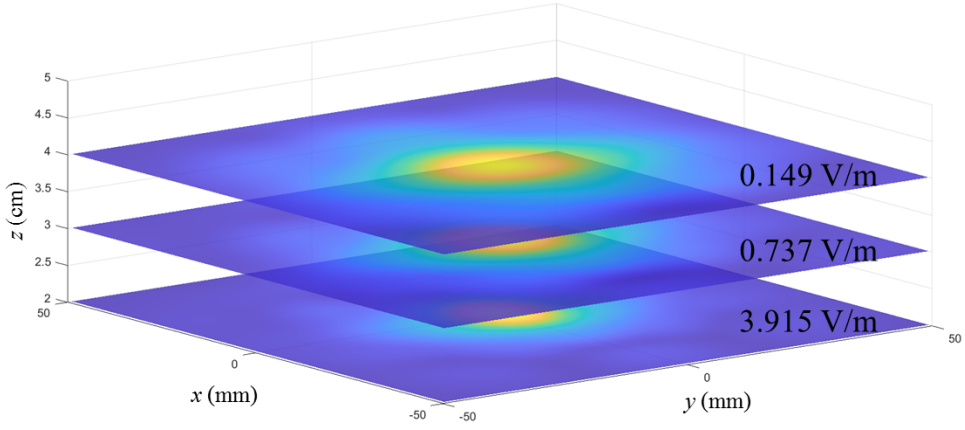

(c) Field distribution at 8 GHz

Fig. 3.25. Normalized near-field plots of the the E-field magnitude of the center element at 3 GHz, 5.5 GHz, and 8 GHz at 2 cm, 3 cm, and 4 cm, with the maximum field values indicated.
Pic credit: Nooshin V. Shahmirzadi.

3.4.2 Performance of edge elements

In the previous section, we observed the performance of an antenna element that is present in the middle of the array. It is also important to analyze the performance of the elements on the border of the prototype. The measurements are done using the same set-up as that of the center element and it is shown in Fig. 3.26.

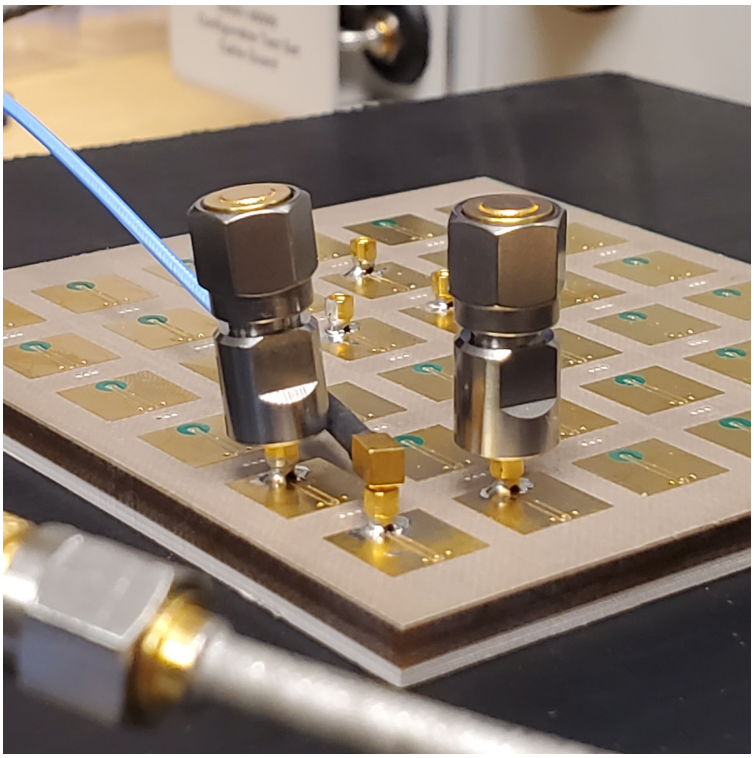

Fig. 3.26. The measurement set-up of the edge element. The corner element is connected to Port 1 of the VNA while the two neighboring elements are loaded with 50 Ohms.

Fig. 3.27a shows the plots of the reflection coefficients of the corner element when its neighbors are loaded with 50 Ohms and when they are left open. It is interesting to note that the input impedance performance is nearly identical in both scenarios, ensuring the good isolation among the array elements. A comparison of the input impedance performance of the center element and the edge element is presented in Fig. 3.27b. It is observed that the edge element performs poorly in comparison to the center element, which is expected. This is due to the fact that the board edge is very close to the corner element as compared to the one in the center. Although not

infinite, the center element still has larger substrate extent in the x and y directions as compared to that of the corner element and hence this difference is comprehensible.

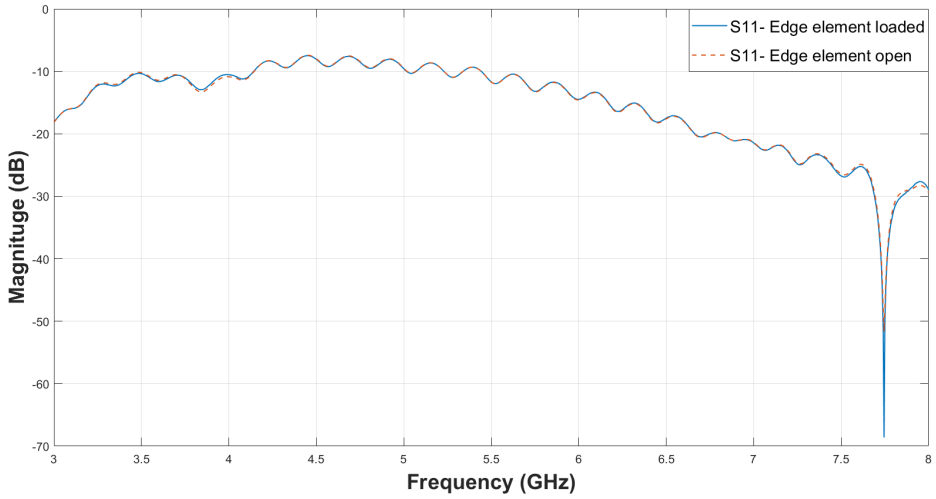

(a)

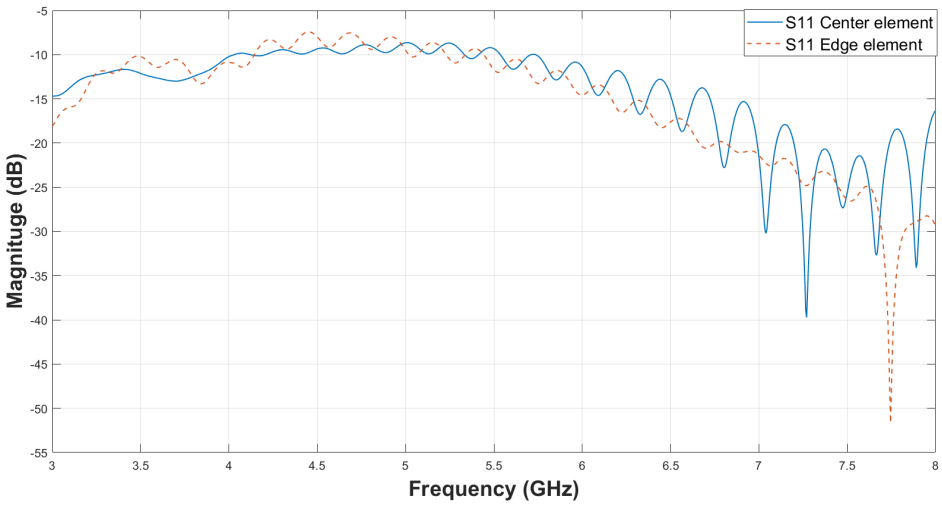

(b)

Fig. 3.27. (a) The reflection coefficients of the edge element with loaded neighboring elements and when they are left open. (b)The reflection coefficients of the center and the edge element when their respective neighbors are loaded with 50 Ohms.

3.4.3 Active element results

To verify the performance of the antenna element in receiving mode through simulations, the excitation needs to be provided at the fork level, as opposed to the transmitting mode, where the excitation is provided by an edge port at the electronics level. To achieve this, the fork is replaced by a port (marked as Port 1 in Fig. 3.28a, consisting of pins P1, P2, and P3). The RF output is at Port 4 (consisting of pins P10 and P11), which is at the electronics layer. The LNA resides between Port 2 and Port 3 as shown in the layout in Fig. 3.28a. To obtain the transmission coefficient S_{21}, *co-simulation* is performed using the *Schematic* part of ADS (see Fig. 3.28b). A two-port network is simulated, where Port 1 is defined between signal pin P1 and ground pins P2 and P3. Port 2 is defined between pin P10 (the signal pin of the SMPS connector) and pin P11 (ground pin). The *S*-parameters of the LNA, provided by the manufacturer, are imported between pin P4 and pin P7.

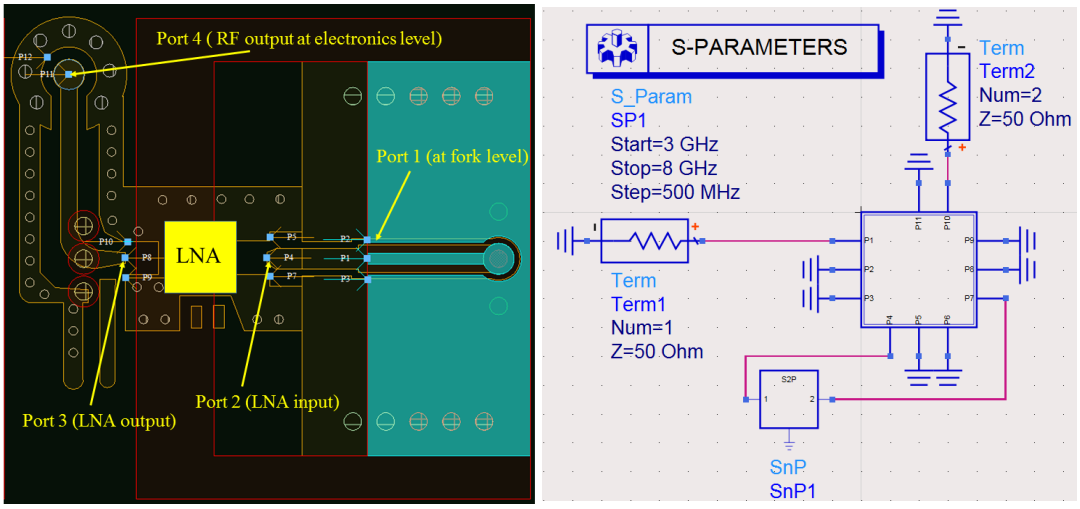

(a) (b)

Fig. 3.28. (a) Electromagnetic (EM) simulation set-up of the active antenna element in the layout. (b) The ADS schematic used for *co-simulation*.

To observe the expected gain from the integration of the LNA, the passive antenna element is also simulated in ADS, for obtaining S_{21} without the LNA. In this simulation the excitation is provided at the fork layer (Port 1), and the output is obtained at the end of CPW (Port 2) at the electronics layer. The average gain of the LNA

(Mini-Circuits PMA3-83LN+), utilized in the design is 20 dB. We can observe from the plots in Fig. 3.29 that the signal is amplified by 20 dB in the frequency range from 3 GHz to 8 GHz, as expected.

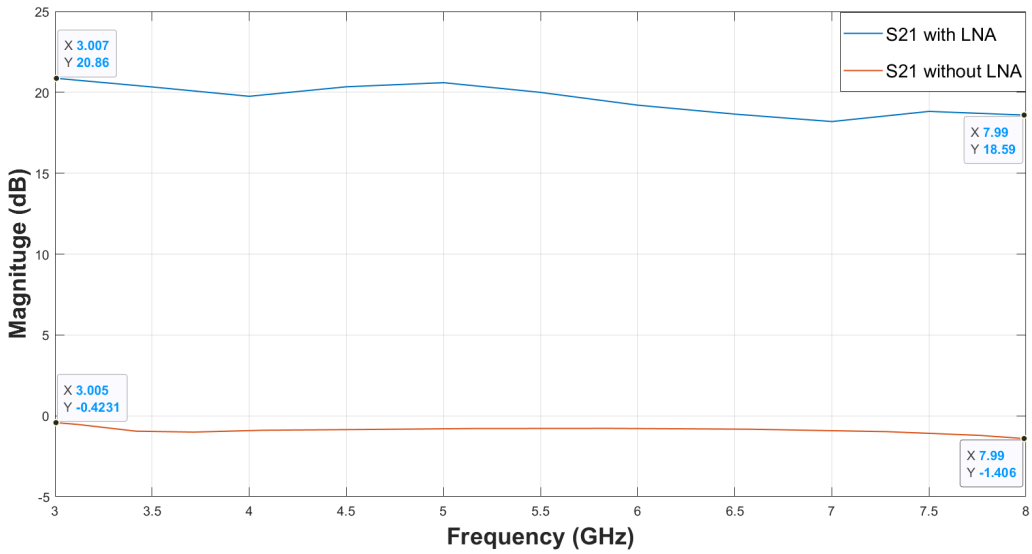

Fig. 3.29. The simulated transmission coefficients S_{21} of the passive and the active antenna element.

Chapter 4

Characterization of High-speed Vertical Connectors

The antenna arrays proposed in [54], [59] and in this thesis, utilize SMPS connectors to access the output (see Fig. 4.1). These connectors as well as their assembly parts such as cables and adapters, are expensive. Moreover, they are mechanically weak and have mating cycles ranging from 100 to 500 depending on the type of interface (full detent or smooth bore) [89]. For an initial investigation of the performance of the array, these connectors can be utilized. However, for our envisioned 18×18 array these connectors are not suitable due to high cost and lack of mechanical strength. The SMA connectors are a low-cost alternative but they are too large for the dense arrangement of the antenna elements in our array. The high-speed vertical connector [61] is investigated as the best alternative, which is cost-effective and mechanically robust compared to the currently used SMPS connectors. This is a 2 mm pitch, edge-card connector with dual row connections. Each row has up to 50 contacts per row as shown in Fig. 4.3. It is a surface mount connector and can accept vertical boards with a thickness of either 1.6 mm or 2.36 mm.

We discussed two strategies in Chapter 2 regarding the design of mixers. One implementation involves two separate boards, one for the active antenna array and the other for the mixer array. These boards will be connected using the vertical high-speed connector as shown in Fig. 4.4. The horizontal board is the active antenna

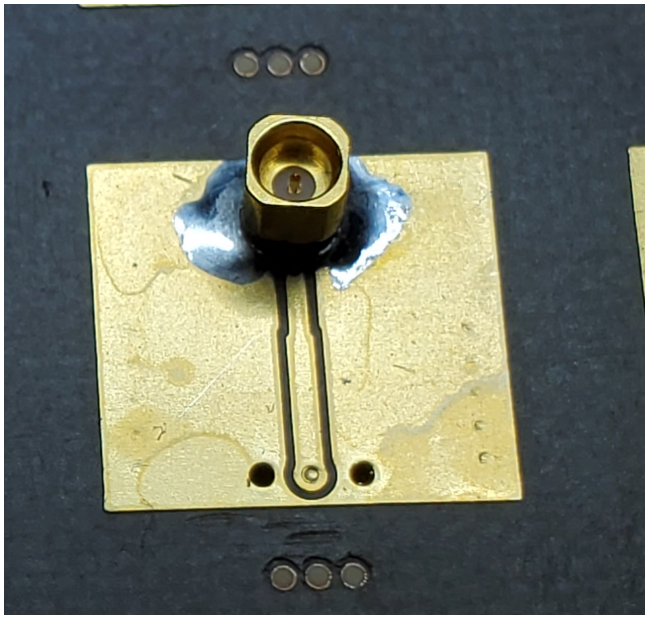

Fig. 4.1. The SMPS connector for accessing the output from the CPW at the electronics layer of the passive antenna array.

Fig. 4.2. The photo shows the two rows of 50 contacts available in the high-speed connector. This side is mounted on a horizontal board. The pad size of these contacts is 1.55×1.1 mm^2 with a pitch of 2 mm.

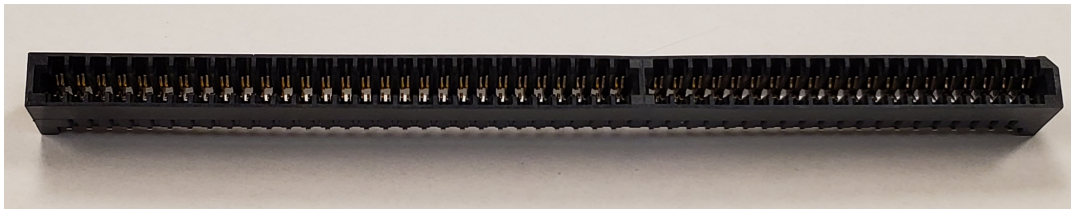

Fig. 4.3. 3-D view of the high-speed connector. Both the horizontal and vertical connections are visible.

array on which the connector is soldered. The mixer array is the vertical board that is inserted into the connector.

In the envisioned system, the output signal from the LNA is fed into the vertical connector and is then vertically transitioned into the mixer board. Before employing this connector in a prototype, its characterization is a must. This is to ensure its usability in the frequency range of interest (3 GHz to 8 GHz). The next section provides a brief introduction to the calibration procedure, followed by the de-embedded

results obtained for the high-speed connector.

4.1 Error de-embedding using TRL method for the high-speed vertical connector

4.1.1 Background on error de-embedding

At microwave frequencies, systematic effects such as leakage, port mismatch and frequency response affect the measured data. However, in a stable measurement environment, these effects are repeatable and can be measured by the network analyzer. This process is called "measurement calibration". During measurement calibration, a series of known standards are connected (such as open, short and load). The systematic effects are determined as the difference between the measured and known responses of the standards. The characterized errors are then found using signal flow graphs. The process of mathematically removing these effects is called 'error correction' or 'error de-embedding'.

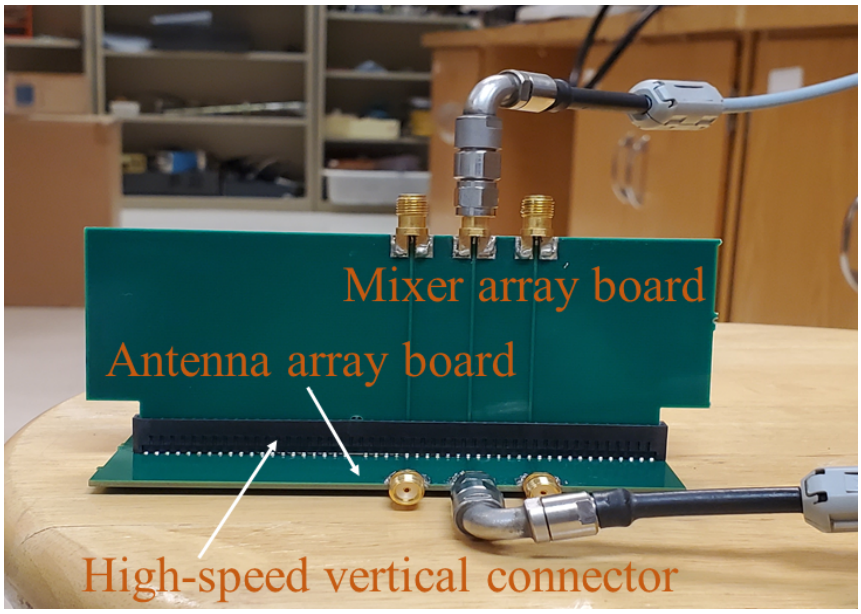

Fig. 4.4. Photo shows the envisioned assembly of the active antenna array board, mixer array board, and high-speed vertical connector.

A major problem encountered when making network measurements in microstrip, or other non-coaxial interconnect is the need to separate the effects of the transmission medium (in which the device is embedded for testing) from the device characteristics. The accuracy of the measurements depends on the availability of quality calibration standards. Unlike coaxial measurements, a set of three distinct impedance standards are often difficult to achieve in the case of non-coaxial transmission lines. For example, in microstrip short terminations are inductive, open terminations radiate and purely resistive wideband loads are difficult to build. For this reason, an alternative calibration approach is needed. The "THRU", "REFLECT" and "LINE" (TRL) calibration technique relies only on the characteristic impedance of the transmission line. Due to its simplicity, TRL can be applied in dispersive transmission media such as microstrip, stripline and waveguide.

4.1.2 TRL calibration

TRL calibration is based on an 8-term error model as shown in Fig. 4.5 [92], [93], [94]. The advantages of using transmission lines as reference standards include easy realization in non-coaxial technology and a characteristic impedance that can be accurately determined from the physical dimensions and the materials. The calibration requires three 2-port custom calibration structures:

- THRU: port 1 and port 2 are connected directly or using a short length of a transmission line.
- REFLECT: each port is loaded with a high reflection termination.
- LINE (or delay): a short length of a transmission line is inserted between the two ports (different line lengths are required for THRU and LINE).

The S-parameter measurements are done using the three TRL standards and the device under test (DUT). The general signal flow graph used for the mathematical modeling of the three TRL standards and the actual DUT is shown in Fig. 4.6. The systematic errors to be calculated are shown as error boxes A and B. In order to

calibrate, the box DUT is replaced with the three TRL standards, resulting in the signal flow graphs shown in Fig. 4.7 to Fig. 4.9.

For THRU measurements, all the S-parameters must be known. For a zero-length THRU, the reflection coefficients are given as $S_{11}^{thru} = S_{22}^{thru} = 0$ and its transmission coefficients are $S_{21}^{thru} = S_{12}^{thru} = 1$. Similarly, for the LINE measurement, two of the S-parameters are known $S_{11}^{line} = S_{22}^{line} = 0$. Lastly, for the REFLECT, we only need to have high reflection coefficients that may or may not be known.

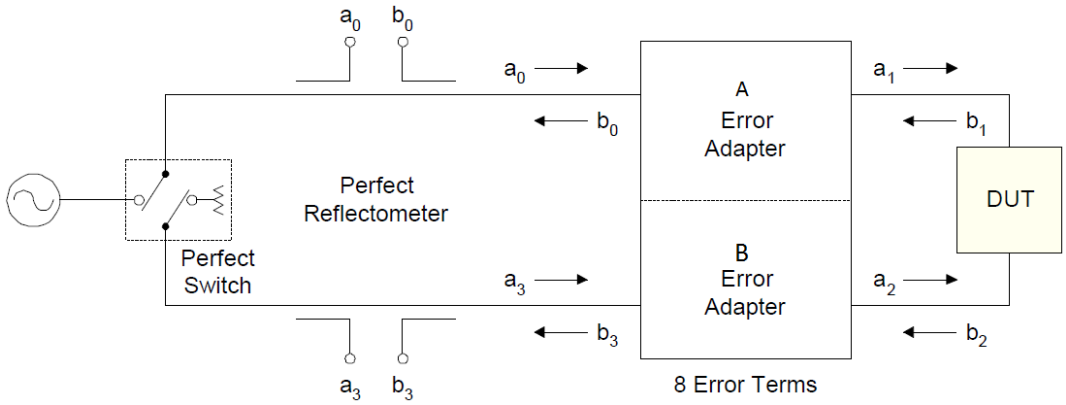

Fig. 4.5. Schematic of the 2-port 8-term error model [94] used in calibration.

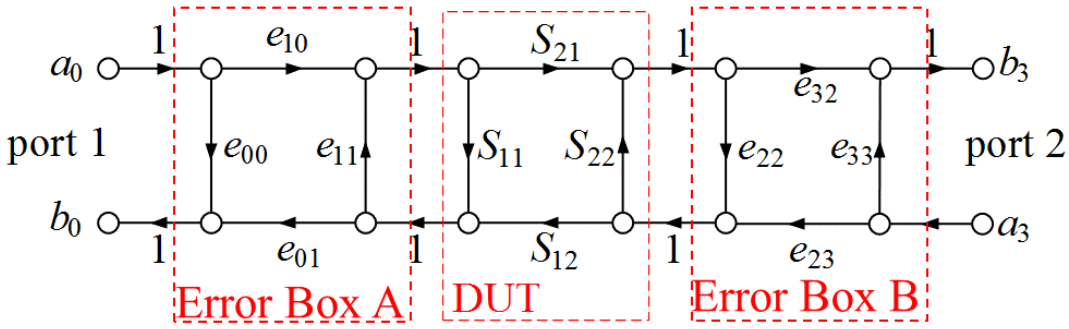

Fig. 4.6. The signal flow graph for an 8-term error model. The graphs show the two error boxes, A and B, on either side at the ports. The middle box represents measured DUT with S-parameters [94].

The measurements of the three calibration standards yield 12 independent equations, with each standard providing 4 equations. In TRL calibration, the scattering matrix is transformed to wave cascading matrix or scattering transfer matrix (T-matrix) [92]. The advantage of using the T-parameters or T-matrix is that the

cascade of two or more two-ports is simply given as the product of the individual transfer matrices. For example the measured output matrix of Fig. 4.7 is $T_A T T_B$. The relationship between the T-matrix and the S-matrix of a device is

$$\begin{bmatrix} T_{11} & T_{12} \\ T_{21} & T_{11} \end{bmatrix} = \frac{1}{S_{21}} \begin{bmatrix} -\Delta & S_{11} \\ -S_{22} & 1 \end{bmatrix} \tag{4.1}$$

Here, $\Delta = S_{11}S_{22} - S_{12}S_{21}$.

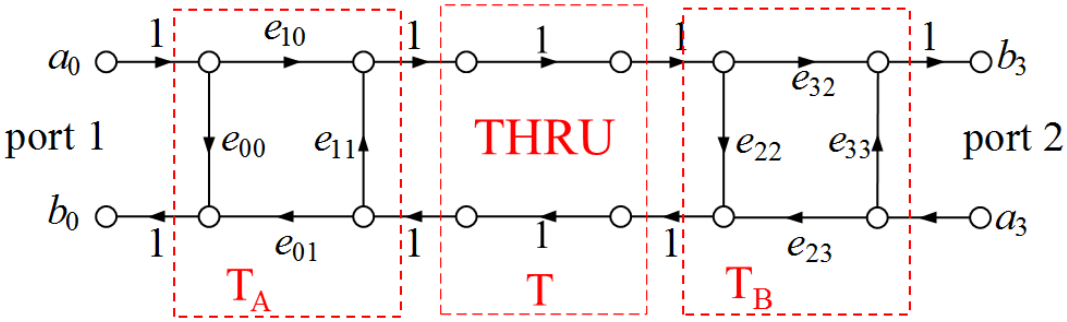

Fig. 4.7. The signal flow graph of the THRU measurement in 8-term error model.

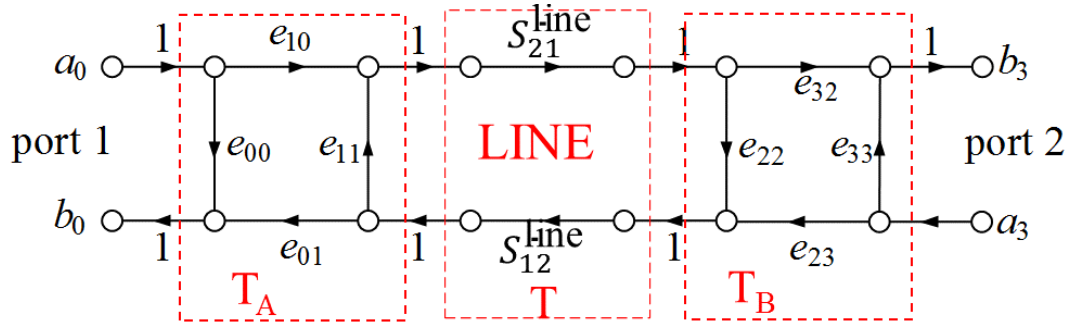

Fig. 4.8. The signal flow graph of the LINE measurement in 8-term error model.

As discussed earlier, the wave cascading matrix of the measured DUT, defined here as T_M is given as the product of the wave cascading matrix of error boxes A and B and the wave cascading matrix of the actual parameters of the DUT (defined here as T) which we want to de-embedd,

$$T_M = T_A T T_B. \tag{4.2}$$

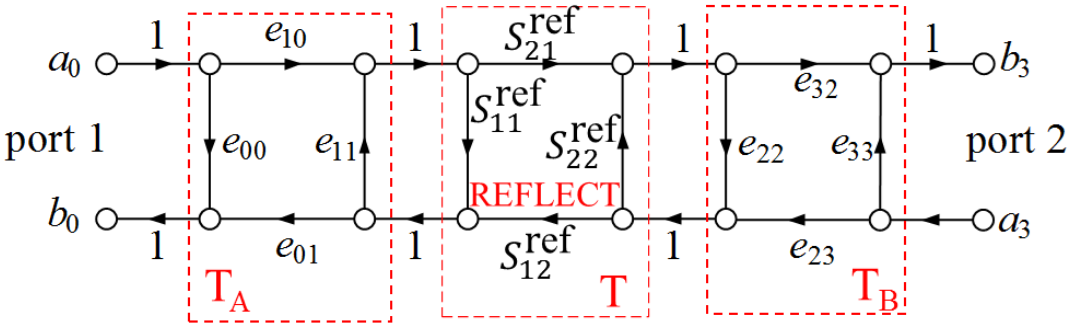

Fig. 4.9. The signal flow graph of the REFLECT measurement in the 8-term error model.

The matrices in (4.2) in terms of their S-parameters are given as:

$$\mathrm{T_M} = \frac{1}{\mathrm{S_{21M}}}\begin{bmatrix} -\Delta_M & S_{11M} \\ -S_{22M} & 1 \end{bmatrix}, \Delta_\mathrm{M} = \mathrm{S_{11M}S_{22M} - S_{12M}S_{21M}}, \tag{4.3}$$

$$\mathrm{T_A} = \frac{1}{\mathrm{e_{10}}}\begin{bmatrix} -\Delta_A & e_{00} \\ -e_{11} & 1 \end{bmatrix}, \Delta_\mathrm{A} = \mathrm{e_{00}e_{11} - e_{10}S_{01}}, \tag{4.4}$$

$$\mathrm{T_B} = \frac{1}{\mathrm{e_{32}}}\begin{bmatrix} -\Delta_B & e_{22} \\ -e_{33} & 1 \end{bmatrix}, \Delta_\mathrm{B} = \mathrm{e_{22}e_{33} - e_{32}S_{23}}. \tag{4.5}$$

Substituting (4.3), (4.4) and(4.5) in (4.2), we get

$$\frac{1}{S_{21M}}\begin{bmatrix} -\Delta_M & S_{11M} \\ -S_{22M} & 1 \end{bmatrix} = \frac{1}{e_{10}e_{32}}\begin{bmatrix} -\Delta_A & e_{00} \\ -e_{11} & 1 \end{bmatrix}\mathrm{T}\begin{bmatrix} -\Delta_B & e_{22} \\ -e_{33} & 1 \end{bmatrix} \tag{4.6}$$

Rearranging (4.2), we obtain

$$\mathrm{T} = \mathrm{T_A}^{-1}\mathrm{T_M}\mathrm{T_B}^{-1}. \tag{4.7}$$

with S-parameters determined by transforming the T-matrix back to the S-matrix. From the structure of (4.6), it is clear that the measured value of S_{21} must be non-zero; similarly $e_{10}e_{32}$ known as the transmission tracking term, must also be non-zero. Another aspect of the eight-term error model is recognition that only seven independent terms are needed to represent the model. The values e_{00}, e_{11}, e_{22} and e_{33}

represent four of the independent values. The values of e_{10}, e_{01}, e_{23} and e_{32} always appear in the error correction as products, $e_{10}e_{01}, e_{10}e_{32}$ and $e_{32}e_{23}$, thus the four terms represent only three independent values. In addition to these seven unknown error terms, the reflection coefficient of the REFLECT standard and the propagation constant of the LINE standard are unknown as well. All of these unknowns can be calculated, using the S-parameter measurements of the three calibration standard and the DUT whose actual parameters are to be error corrected (high-speed connector in this case).

4.1.2.1 Design considerations for TRL standard prototype

The following design considerations are used when designing the TRL standards:

- The THRU standard can be either a zero-length or non-zero length transmission line. However, a zero-length THRU is more accurate because it has zero loss and no reflections, by definition.
- The THRU standard cannot be the same electrical length as the LINE standard.
- The REFLECT standard can be anything with a high reflection as long as it is the same when connected to both VNA ports. The actual magnitude of the reflection need not be known. If the magnitude and phase of the reflection standard are well-defined, the standard may be used to set the reference plane.
- The LINE standard must be of the same impedance and propagation constant as the THRU standard.
- A single LINE standard is only usable over an 8:1 frequency range, which in this case is the ratio of upper to lower frequency. Therefore, for broad frequency coverage, multiple lines are required.
- The LINE standard must be an appropriate electrical length for the frequency range: at each frequency, the phase difference between the THRU and the LINE should be greater than 20°s and less than 160°.

- The LINE standard must have a delay that is greater than zero ps. Otherwise, calibration correction calculations contain unpredictable results.
- The optimal length of the LINE standard is 1/4 wavelength at the geometric mean of the frequency span (square root of f1 (lower frequency limit for which calibration is needed) x f2 (upper frequency limit for which calibration is needed)).

The designed TRL standards (in *ALTIUM DESIGNER* [95]) along with the evaluation boards for the high-speed connector are shown in Fig. 4.10.

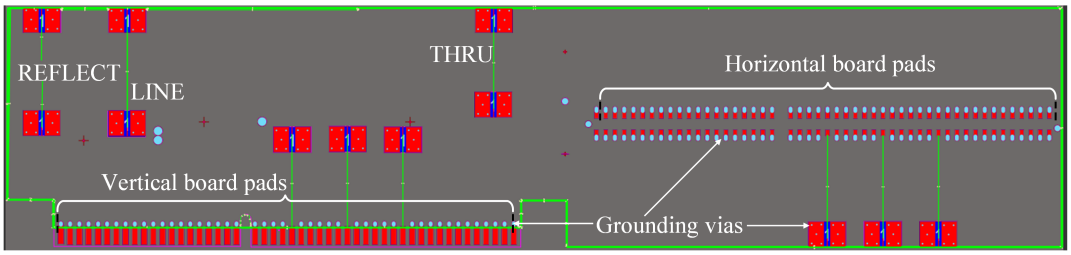

Fig. 4.10. The schematic of the designed prototype (in *ALTIUM DESIGNER* [95]) showing both the TRL standards and the evaluation boards (vertical and horizontal).

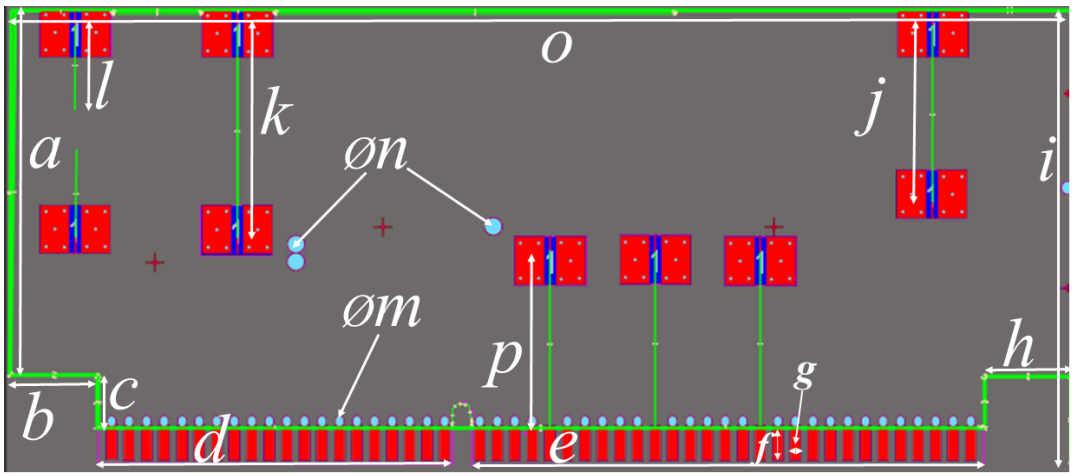

Fig. 4.11. The layout of the vertical connector evaluation board along with the designed TRL calibration standards.

The TRL calibration standards and the evaluation boards are printed on an FR408HR substrate with ϵ_r = 3.68 and tan δ = 0.0092 and a height of 0.1702 mm. The prototype is a four-layer board with a thickness of 1.6 mm, which satisfies the requirement

for the thickness of the vertical board, which can be inserted into the connector. The THRU is of length 20 mm, while the LINE is designed to be 24 mm. All the traces on the board have a width of 0.354 mm for a 50 Ohm characteristic impedance. The phase difference between the THRU and the LINE standards is 24.38° at 3 GHz, and it is 65° at 8 GHz. The phase differences lie between the desired range from 20° to 160°. The board dimensions are marked in Fig. 4.11 and Fig. 4.12, and their values are provided in Table 4.1.

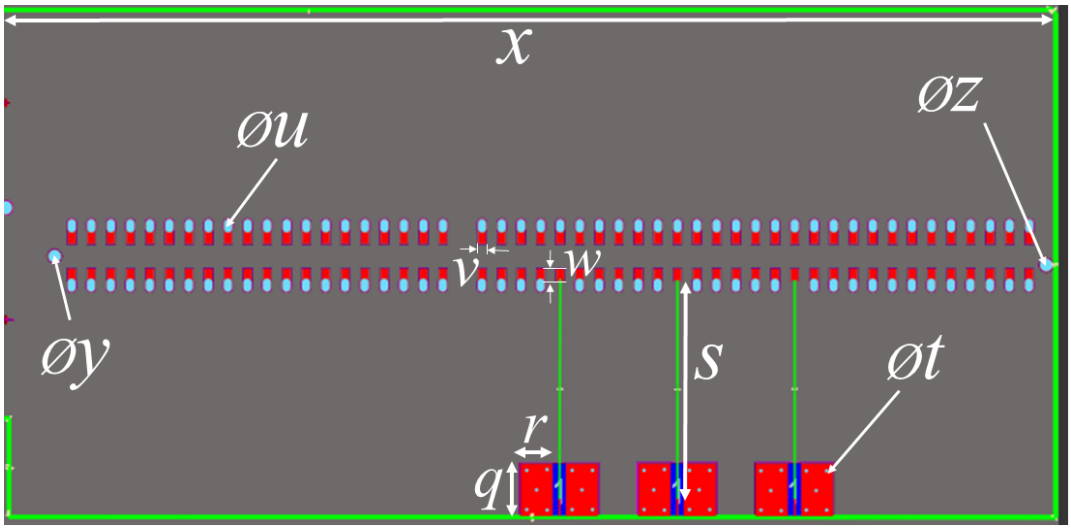

Fig. 4.12. The layout of the horizontal connector evaluation board.

Table 4.1. Dimensions of the designed evaluation boards and the TRL standards.

Symbol	Size	Symbol	Size
a	41.000mm	*n*	2.000mm
b	9.779mm	*o*	120.52mm
c	5.969mm	*p*	21.417mm
d	40.132mm	*q*	5.742mm
e	58.166mm	*r*	3.653mm
f	1.250mm	*s*	22.477mm
g	1.250mm	*t*	0.508mm
h	9.398mm	*u*	1.499mm
i	51.435mm	*v*	1.100mm
j	20.000mm	*w*	1.553mm
k	24.000mm	*x*	107.442mm
l	10.000mm	*y*	1.450mm
m	1.250mm	*z*	1.653mm

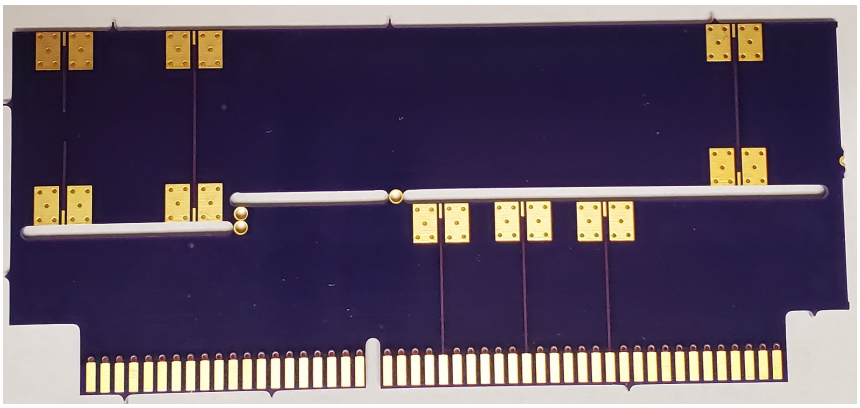

(a)

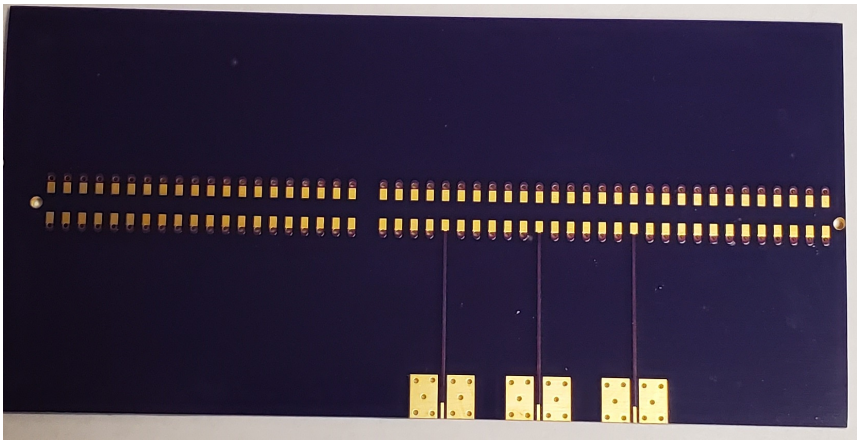

(b)

Fig. 4.13. Photos of the fabricated prototypes of the evaluation boards: (a) vertical board along with the TRL standards and (b) horizontal board.

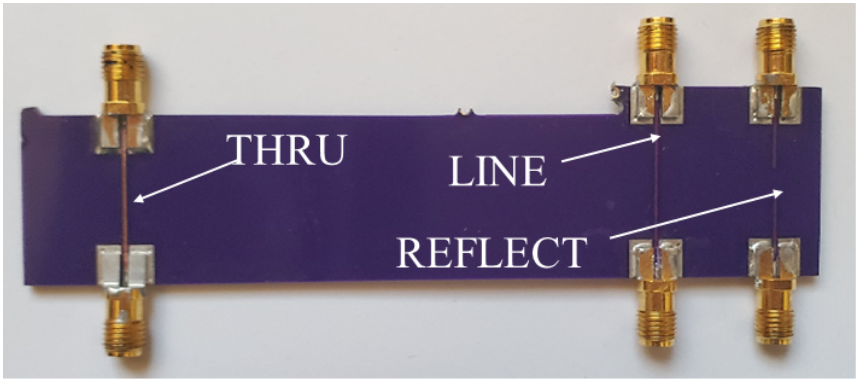

Fig. 4.14. Photo of the TRL standards printed on a PCB. The standards are connectorized with SMA connectors.

4.2 Error de-embedding results

To execute the error de-embedding, the method reported in [96] is adopted. The detailed explanation of the method is presented in Appendix A and the MATLAB code used for error de-embedding is given in Appendix B. First, the S-parameters of the three TRL standards and the vertical connector (with measurement set-up shown in Fig. 4.4) are measured with the vector network analyzer. The obtained S-parameters from the measurements (the TRL standards and the vertical connector) are then converted to T-parameters and using the code, the actual parameters of the vertical connector are de-embedded. To verify that the code is working accurately, we first obtain the de-embedded S-parameters of the THRU standard. We compared the known results with the one obtained after de-embedding (see Fig. 4.15) to validate the accuracy of the code.

Fig. 4.15 shows the de-embedded transmission coefficient of the THRU standard. It is one, which is the expected result for a through transmission line. Also, the obtained reflection coefficient satisfies the requirement for the standard. Once, the code is validated, the S-parameters of high-speed connector are extracted using the code. The obtained error-corrected S-parameters of the high-speed connector are shown in Fig. 4.16. From Fig. 4.16a, we can observe that the reflection coefficient lies below -10 dB from 3 GHz to 7 GHz. Above 7 GHz, the response of the connector deteriorates and it is approximately -7 dB at 8 GHz. This value, although sub-standard, is still acceptable. The effect of the calibration is evident from Fig. 4.16b. After de-embedding, a clear improvement in the transmission coefficient is observed.

From the characterization of the high-speed connector reported here, it can be concluded that it is suitable as an inter-connection between the active antenna array and the mixer array in the envisioned system architecture.

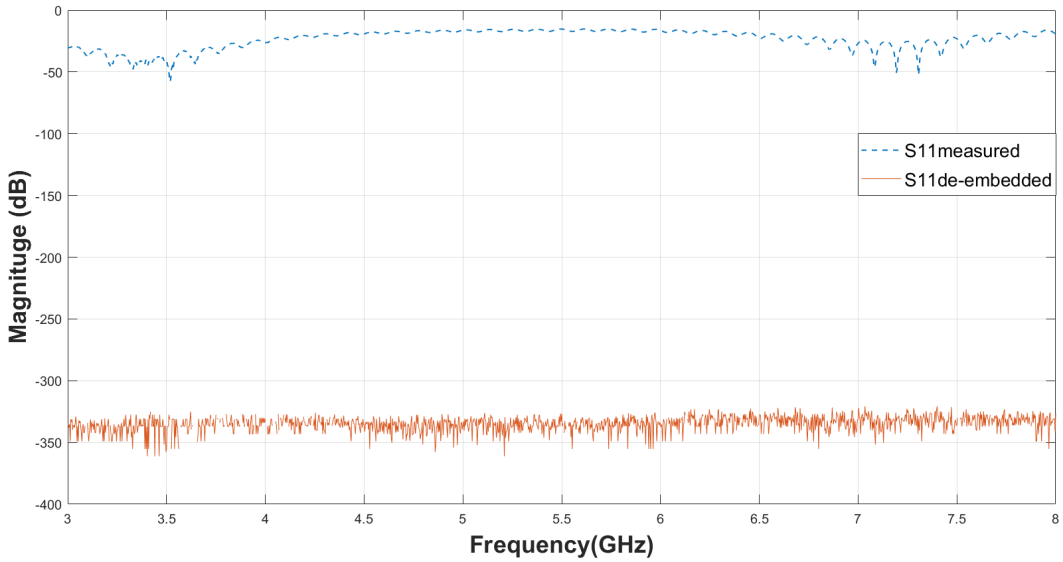

(a)

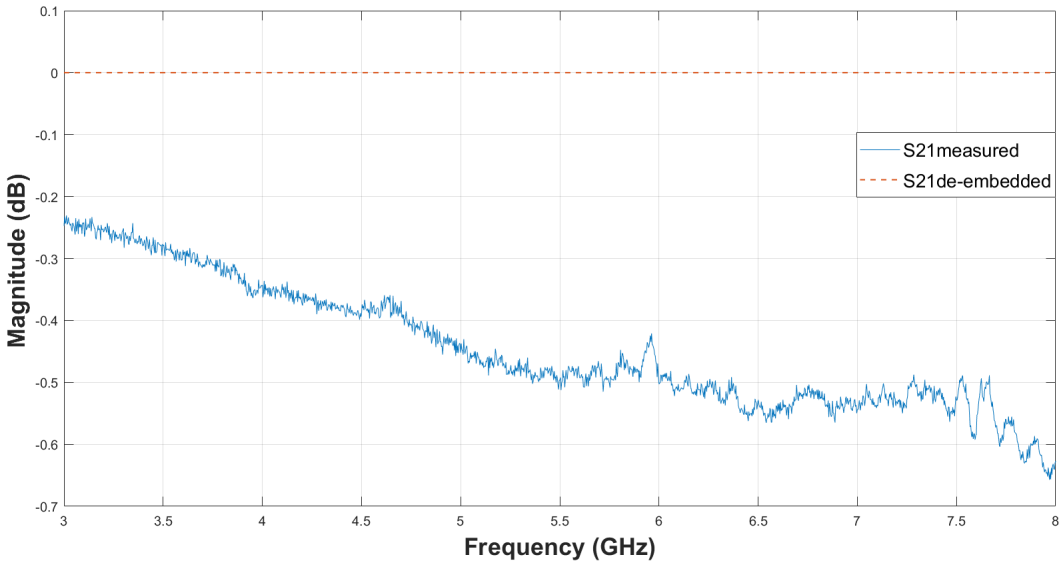

(b)

Fig. 4.15. The plots show: (a) the measured and the de-embedded reflection coefficients of the TRHU standard, and (b) the measured and the de-embedded transmission coefficients of the TRHU standard.

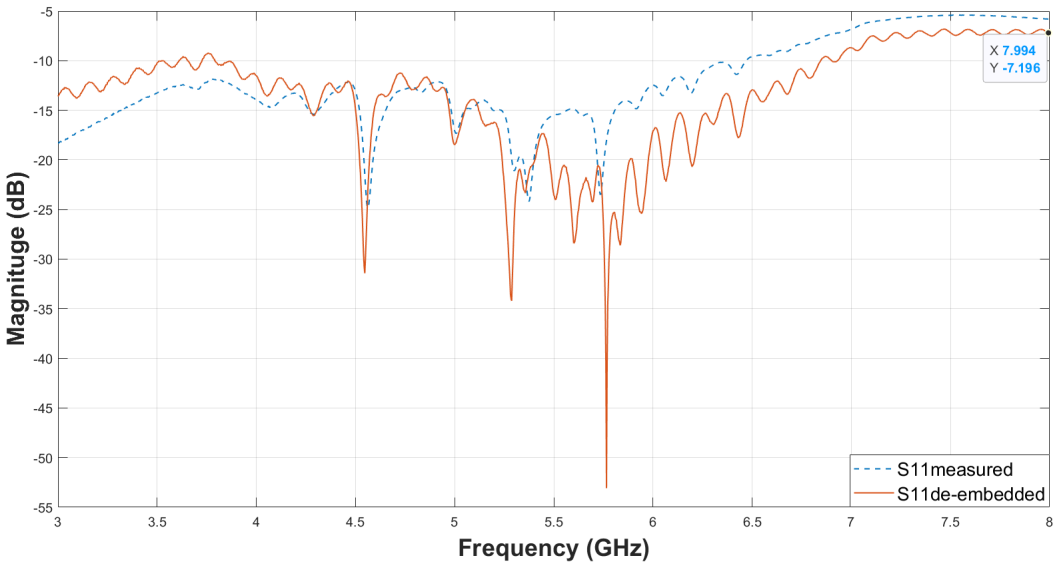

(a)

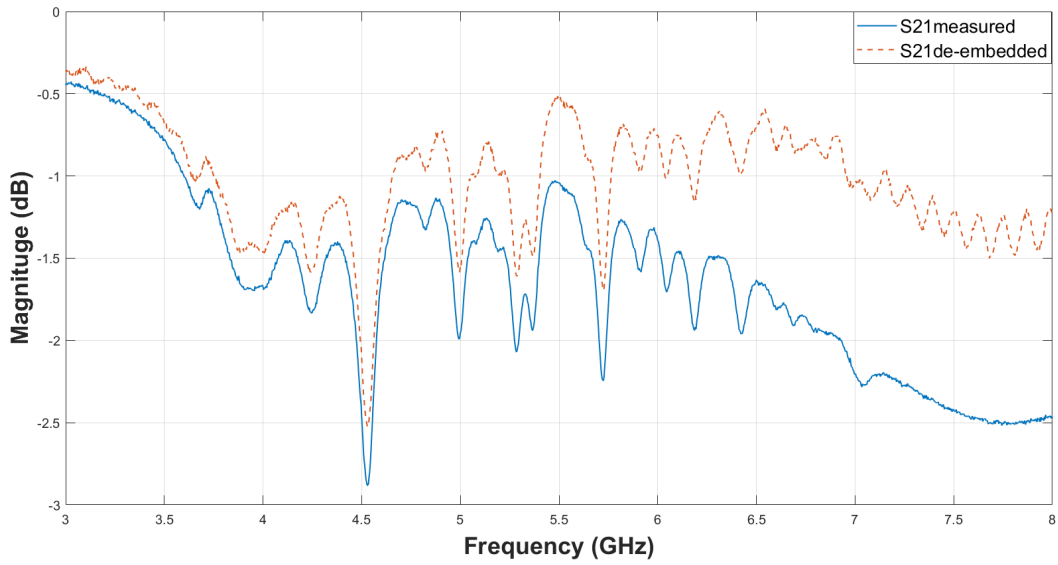

(b)

Fig. 4.16. The plots show: (a) the measured and the de-embedded reflection coefficients of the high-speed connector, and (b) the measured and the de-embedded transmission coefficients of the high-speed connector.

Chapter 5

Conclusion and Future work

An active antenna sensor array for microwave imaging of the breast is developed. A complete isolation of the antennas from the electronics using a shielding layer within the multi-layer array PCB is reported. The passive antenna array (the array before integrating the LNA), is fabricated and measured. A reflection coefficient lower than -10 dB is obtained from 3 GHz to 8 GHz in the simulated design. On the other hand, the measured reflection coefficient is below -10 dB for all of the frequency band of interest (3 GHz to 8 GHz) except from 4 GHz to 5.5 GHz, where it grazes just above the -10 dB threshold. The mutual coupling between the antenna elements is below -20 dB in both the simulations and the measured results. Deviation is reported between the simulations and measurements. The differences between the simulated and measured results stem from errors due to port modeling, differences in the tissue permittivity (in simulations it is constant over the entire frequency band, whereas in carbon-rubber tissue phantoms it is frequency-dependent), array size and the inability of the calibration to take into account the SMPS connectors of the cables. The simulated active antenna element shows an expected gain of 20 dB from 3 GHz to 8 GHz.

The vertical high-speed connector interfacing the active antenna array with the array of mixers is characterized. Its transmission coefficients have been measured and shown to be excellent from 3 GHz to 7 GHz and acceptable from 7 GHz to 8 GHz.

5.1 Recent findings

The simulation results reported in Chapter 3 consider a constant tissue permittivity ($\epsilon_r = 10.2$, $\tan\delta = 0.5$) over the entire bandwidth in an adaptive frequency sweep. To achieve more realistic results, the simulations are repeated in FEKO using discrete frequency sweep. This allows for the tissue permittivity to be defined at each frequency point using the data from Fig. 3.20. The comparison between the adaptive simulation, the measured results, and the results from discrete-frequency simulation are shown in Fig. 5.1. It is observed that the discrete-frequency simulation is better matched to the measured results as compared to the adaptive simulation, which is expected as we employ frequency-dependent phantom permittivity as opposed to the frequency-independent permittivity used in the adaptive simulations.

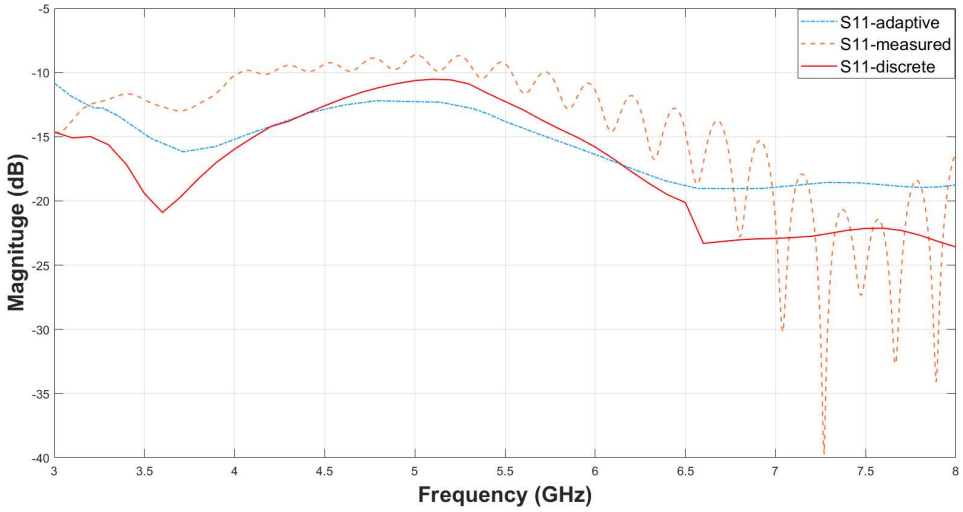

Fig. 5.1. Comparison between the adaptive simulation, discrete simulation, and measured results.

Acknowledgement: The results of the discrete simulations are provided by N. V. Shahmirzade.

5.2 Recommendation for future work

(i) Fabrication and measurement of the active antenna array is the immediate task to be undertaken (the boards are being fabricated at the time of writing this thesis) to verify the results obtained from simulation.

(ii) The future simulations must be carried out using discrete-frequency sweeps that employ the measured carbon-rubber tissue-phantom permittivity, in order to obtain reliable results that agree better with measurements .

(iii) The integration of the high-speed connector with an 18×18 active antenna array must be carried out and respective prototype must be measured.

(iv) The design and fabrication of the vertical mixer-array board, which will be loaded into the high-speed connector, are required. Its performance must be tested together with the active antenna array and the vertical connector. The first mixer array will employ wired LO signal input.

(v) Further miniaturization of the antenna element to achieve a center-to-center distance of 10 mm can be carried out. However, at this inter-element spacing the antenna becomes electrically small with the antenna size dropping below $\lambda/3$ at 3 GHz and thus this will pose a significant design challenge.

(vi) Investigating the placement of the array in a shielding enclosure to further reduce the interference at the electronics layer is another task that needs to be carried out in the future.

Bibliography

[1] C. C. Society, "Breast cancer statistics," 2020. [Online]. Available: https://www.cancer.ca/en/cancer-information/cancer-type/breast/statistics/?region=on

[2] W. A. Berg, L. Gutierrez, M. S. NessAiver, W. B. Carter, M. Bhargavan, R. S. Lewis, and O. B. Ioffe, "Diagnostic accuracy of mammography, clinical examination, US, and MR imaging in preoperative assessment of breast cancer," *Radiology*, vol. 233, no. 3, pp. 830–849, 2004.

[3] I. U. P. on Breast Cancer Screening and Others, "The benefits and harms of breast cancer screening: An independent review," *The Lancet*, vol. 380, pp. 1778–1786, 2012.

[4] A. B. de Gonzalez and S. Darby, "Risk of cancer from diagnostic X-rays: estimates for the UK and 14 other countries," *The Lancet*, vol. 363, no. 9406, pp. 345–351, 2004.

[5] C. M. Ronckers, C. A. Erdmann, and C. E. Land, "Radiation and breast cancer: a review of current evidence," *Breast Cancer Research*, vol. 7, no. 1, pp. 1–12, 2004.

[6] A. Moore, "The practice of breast ultrasound: techniques, findings, differential diagnosis," *Ultrasound in Medicine and Biology*, vol. 36, no. 2, p. 358, 2010.

[7] S. Kwon and S. Lee, "Recent advances in microwave imaging for breast cancer detection," *International Journal of Biomedical Imaging*, vol. 2016, 2016.

[8] S. G. Orel and M. D. Schnall, "Mr imaging of the breast for the detection, diagnosis, and staging of breast cancer," *Radiology*, vol. 220, no. 1, pp. 13–30, 2001.

[9] S. Chaudhary, R. Mishra, A. Swarup, and J. M. Thomas, "Dielectric properties of normal & malignant human breast tissues at radiowave & microwave frequencies," *Indian Journal of Biochemistry & Biophysics*, vol. 21, no. 1, pp. 76–79, 1984.

[10] N. K. Nikolova, "Microwave imaging for breast cancer," *IEEE Microwave Magazine*, vol. 12, no. 7, pp. 78–94, 2011.

[11] A. J. Surowiec, S. S. Stuchly, J. R. Barr, and A. Swarup, "Dielectric properties of breast carcinoma and the surrounding tissues," *IEEE Transactions on Biomedical Engineering*, vol. 35, no. 4, pp. 257–263, 1988.

[12] A. Campbell and D. Land, "Dielectric properties of female human breast tissue measured in vitro at 3.2 ghz," *Physics in Medicine & Biology*, vol. 37, no. 1, p. 193, 1992.

[13] W. T. Joines, Y. Zhang, C. Li, and R. L. Jirtle, "The measured electrical properties of normal and malignant human tissues from 50 to 900 mhz," *Medical Physics*, vol. 21, no. 4, pp. 547–550, 1994.

[14] J. W. Choi, J. Cho, Y. Lee, J. Yim, B. Kang, K. K. Oh, W. H. Jung, H. J. Kim, C. Cheon, H.-D. Lee *et al.*, "Microwave detection of metastasized breast cancer cells in the lymph node; potential application for sentinel lymphadenectomy," *Breast Cancer Research and Treatment*, vol. 86, no. 2, pp. 107–115, 2004.

[15] M. Lazebnik, D. Popovic, L. McCartney, C. B. Watkins, M. J. Lindstrom, J. Harter, S. Sewall, T. Ogilvie, A. Magliocco, T. M. Breslin *et al.*, "A large-scale study of the ultrawideband microwave dielectric properties of normal, benign and malignant breast tissues obtained from cancer surgeries," *Physics in Medicine & Biology*, vol. 52, no. 20, p. 6093, 2007.

[16] R. J. Halter, T. Zhou, P. M. Meaney, A. Hartov, R. J. Barth Jr, K. M. Rosenkranz, W. A. Wells, C. A. Kogel, A. Borsic, E. J. Rizzo *et al.*, "The correlation of in vivo and ex vivo tissue dielectric properties to validate electromagnetic breast imaging: initial clinical experience," *Physiological Measurement*, vol. 30, no. 6, p. S121, 2009.

[17] T. Sugitani, S.-i. Kubota, S.-i. Kuroki, K. Sogo, K. Arihiro, M. Okada, T. Kadoya, M. Hide, M. Oda, and T. Kikkawa, "Complex permittivities of breast tumor tissues obtained from cancer surgeries," *Applied Physics Letters*, vol. 104, no. 25, p. 253702, 2014.

[18] A. Martellosio, M. Pasian, M. Bozzi, L. Perregrini, A. Mazzanti, F. Svelto, P. Summers, G. Renne, and M. Bellomi, "0.5–50 ghz dielectric characterisation of breast cancer tissues," *Electronics Letters*, vol. 51, no. 13, pp. 974–975, 2015.

[19] Y. Cheng and M. Fu, "Dielectric properties for non-invasive detection of normal, benign, and malignant breast tissues using microwave theories," *Thoracic Cancer*, vol. 9, no. 4, pp. 459–465, 2018.

[20] L. E. Larsen and J. H. Jacobi, "Microwave interrogation of dielectric targets. part i: By scattering parameters," *Medical Physics*, vol. 5, no. 6, pp. 500–508, 1978.

[21] J. H. Jacobi and L. E. Larsen, "Microwave interrogation of dielectric targets. part ii: By microwave time delay spectroscopy," *Medical Physics*, vol. 5, no. 6, pp. 509–513, 1978.

[22] R. W. Deming and A. J. Devaney, "Diffraction tomography for multi-monostatic ground penetrating radar imaging," *Inverse Problems*, vol. 13, no. 1, p. 29, 1997.

[23] E. C. Fear and J. M. Sill, "Preliminary investigations of tissue sensing adaptive radar for breast tumor detection," in *Proceedings of the 25th Annual Interna-*

tional Conference of the IEEE Engineering in Medicine and Biology Society (IEEE Cat. No. 03CH37439), vol. 4. IEEE, 2003, pp. 3787–3790.

[24] E. C. Fear, J. Sill, and M. A. Stuchly, "Experimental feasibility study of confocal microwave imaging for breast tumor detection," *IEEE Transactions on Microwave Theory and Techniques*, vol. 51, no. 3, pp. 887–892, 2003.

[25] P. Kosmas, Y. Wang, and C. M. Rappaport, "Three-dimensional fdtd model for gpr detection of objects buried in realistic dispersive soil," in *Detection and Remediation Technologies for Mines and Minelike Targets VII*, vol. 4742. International Society for Optics and Photonics, 2002, pp. 330–338.

[26] T. B. Hansen and P. M. Johansen, "Inversion scheme for ground penetrating radar that takes into account the planar air-soil interface," *IEEE Transactions on Geoscience and Remote sensing*, vol. 38, no. 1, pp. 496–506, 2000.

[27] R. Nilavalan, A. Gbedemah, I. J. Craddock, X. Li, and S. C. Hagness, "Numerical investigation of breast tumour detection using," *Electronics Letters*, vol. 39, no. 25, pp. 1787–1789, 2003.

[28] P. M. Meaney, K. D. Paulsen, A. Hartov, and R. K. Crane, "An active microwave imaging system for reconstruction of 2-d electrical property distributions," *IEEE Transactions on Biomedical Engineering*, vol. 42, no. 10, pp. 1017–1026, 1995.

[29] I. Craddock, R. Nilavalan, J. Leendertz, A. Preece, and R. Benjamin, "Experimental investigation of real aperture synthetically organised radar for breast cancer detection," in *2005 IEEE Antennas and Propagation Society International Symposium*, vol. 1. IEEE, 2005, pp. 179–182.

[30] A. Vander Vorst, A. Rosen, and Y. Kotsuka, *RF/microwave interaction with biological tissues*. Wiley Online Library, 2006, vol. 181.

[31] S. C. Hagness, A. Taflove, and J. E. Bridges, "Two-dimensional fdtd analysis of a pulsed microwave confocal system for breast cancer detection: Fixed-focus

and antenna-array sensors," *IEEE Transactions on Biomedical Engineering*, vol. 45, no. 12, pp. 1470–1479, 1998.

[32] E. C. Fear and M. A. Stuchly, "Microwave system for breast tumor detection," *IEEE Microwave and Guided Wave Letters*, vol. 9, no. 11, pp. 470–472, 1999.

[33] D. Hailu, N. Nikolova, and M. Bakr, "Sub-wavelength microwave radar imaging for detection of breast cancer tumors," in *2007 International Symposium on Signals, Systems and Electronics*. IEEE, 2007, pp. 107–110.

[34] E. C. Fear, X. Li, S. C. Hagness, and M. A. Stuchly, "Confocal microwave imaging for breast cancer detection: Localization of tumors in three dimensions," *IEEE Transactions on Biomedical Engineering*, vol. 49, no. 8, pp. 812–822, 2002.

[35] R. Nilavalan, J. Leendertz, I. Craddock, A. Preece, and R. Benjamin, "Numerical analysis of microwave detection of breast tumours using synthetic focussing techniques," in *IEEE Antennas and Propagation Society Symposium, 2004.*, vol. 3. IEEE, 2004, pp. 2440–2443.

[36] W. C. Khor, H. Wang, M. E. Bialkowski, A. Abbosh, and N. Seman, "An experimental and theoretical investigation into capabilities of a uwb microwave imaging radar system to detect breast cancer," in *EUROCON 2007-The International Conference on" Computer as a Tool"*. IEEE, 2007, pp. 771–776.

[37] W. Liu, H. Jafari, S. Hranilovic, and M. Deen, "Time domain analysis of uwb breast cancer detection," in *23rd Biennial Symposium on Communications, 2006*. IEEE, 2006, pp. 336–339.

[38] D. Li, P. M. Meaney, T. Raynolds, S. A. Pendergrass, M. W. Fanning, and K. D. Paulsen, "Parallel-detection microwave spectroscopy system for breast imaging," *Review of Scientific Instruments*, vol. 75, no. 7, pp. 2305–2313, 2004.

[39] S. Y. Semenov, A. E. Bulyshev, A. Abubakar, V. G. Posukh, Y. E. Sizov, A. E. Souvorov, P. M. van den Berg, and T. C. Williams, "Microwave-tomographic imaging of the high dielectric-contrast objects using different

image-reconstruction approaches," *IEEE Transactions on Microwave Theory and Techniques*, vol. 53, no. 7, pp. 2284–2294, 2005.

[40] N. K. Nikolova, *Introduction to microwave imaging*. Cambridge University Press, 2017.

[41] P. Hashemzadeh, A. Fhager, R. Kopecky, L. Bååth, and M. Persson, "Experimental results of an optimization approach to two dimensional time domain electromagnetic inverse problem with application to microwave breast tomography," in *Third IASTED International Conference on Biomedical Engineering, February 16-18, 2005, Innsbruck, Austria*. Acta Press, 2005, pp. 192–196.

[42] L. Jofre, M. S. Hawley, A. Broquetas, E. de Los Reyes, M. Ferrando, and A. R. Elias-Fuste, "Medical imaging with a microwave tomographic scanner," *IEEE Transactions on Biomedical Engineering*, vol. 37, no. 3, pp. 303–312, 1990.

[43] D. Tajik, J. Trac, and N. K. Nikolova, "Quality control of microwave equipment for tissue imaging," *IEEE Journal of Electromagnetics, RF and Microwaves in Medicine and Biology*, vol. 4, no. 1, pp. 52–60, 2019.

[44] R. K. Amineh, M. Ravan, A. Khalatpour, and N. K. Nikolova, "Three-dimensional near-field microwave holography using reflected and transmitted signals," *IEEE Transactions on Antennas and Propagation*, vol. 59, no. 12, pp. 4777–4789, 2011.

[45] R. K. Amineh, J. J. McCombe, A. Khalatpour, and N. K. Nikolova, "Microwave holography using point-spread functions measured with calibration objects," *IEEE Transactions on Instrumentation and Measurement*, vol. 64, no. 2, pp. 403–417, 2014.

[46] H. Zhang, "Microwave imaging for breast cancer detection: The discrimination of breast lesion morphology," *IEEE Access*, vol. 8, pp. 107 103–107 111, 2020.

[47] M. Klemm, D. Gibbins, J. Leendertz, T. Horseman, A. Preece, R. Benjamin, and I. Craddock, "Development and testing of a 60-element uwb conformal ar-

ray for breast cancer imaging," in *Proceedings of the 5th European Conference on Antennas and Propagation (EUCAP)*. IEEE, 2011, pp. 3077–3079.

[48] A. W. Preece, I. Craddock, M. Shere, L. Jones, and H. L. Winton, "Maria m4: clinical evaluation of a prototype ultrawideband radar scanner for breast cancer detection," *Journal of Medical Imaging*, vol. 3, no. 3, p. 033502, 2016.

[49] H. Song, S. Sasada, T. Kadoya, M. Okada, K. Arihiro, X. Xiao, and T. Kikkawa, "Detectability of breast tumor by a hand-held impulse-radar detector: performance evaluation and pilot clinical study," *Scientific Reports*, vol. 7, no. 1, pp. 1–11, 2017.

[50] J.-C. Bolomey and F. E. Gardiol, *Engineering applications of the modulated scatterer technique*. Artech House, 2001.

[51] M. Ostadrahimi, M. Asefi, J. LoVetri, G. E. Bridges, and L. Shafai, "An MST-based microwave tomography system using homodyne receiver," in *2013 IEEE Antennas and Propagation Society International Symposium (APSURSI)*. IEEE, 2013, pp. 814–815.

[52] D. A. Crocker and K. M. Donnell, "Application of electrically invisible antennas to the modulated scatterer technique," *IEEE Transactions on Instrumentation and Measurement*, vol. 64, no. 12, pp. 3526–3535, 2015.

[53] M. A. Abou-Khousa, M. T. Ghasr, S. Kharkovsky, D. Pommerenke, and R. Zoughi, "Modulated elliptical slot antenna for electric field mapping and microwave imaging," *IEEE Transactions on Antennas and Propagation*, vol. 59, no. 3, pp. 733–741, 2010.

[54] F. Foroutan and N. K. Nikolova, "Active sensor for microwave tissue imaging with bias-switched arrays," *Sensors*, vol. 18, no. 5, p. 1447, 2018.

[55] P. M. Meaney, M. W. Fanning, D. Li, S. P. Poplack, and K. D. Paulsen, "A clinical prototype for active microwave imaging of the breast," *IEEE Transactions on Microwave Theory and Techniques*, vol. 48, no. 11, pp. 1841–1853, 2000.

[56] S. P. Poplack, K. D. Paulsen, A. Hartov, P. M. Meaney, B. W. Pogue, T. D. Tosteson, M. R. Grove, S. K. Soho, and W. A. Wells, "Electromagnetic breast imaging: average tissue property values in women with negative clinical findings," *Radiology*, vol. 231, no. 2, pp. 571–580, 2004.

[57] N. K. Nikolova, F. Foroutan, V. Tyagi, C. H. Chen, and C. Baard, "UWB planar bias-switched imaging array for breast-cancer screening," in *Proceedings of the 14th European Conference on Antennas and Propagation (EUCAP)*. IEEE, 2020.

[58] T. Sugitani, S. Kubota, A. Toya, X. Xiao, and T. Kikkawa, "A compact 4×4 planar UWB antenna array for 3-d breast cancer detection," *IEEE Antennas and Wireless Propagation Letters*, vol. 12, pp. 733–736, 2013.

[59] F. Foroutan and N. K. Nikolova, "UWB active antenna for microwave breast imaging sensing arrays," *IEEE Antennas and Wireless Propagation Letters*, vol. 18, no. 10, pp. 1951–1955, 2019.

[60] Mini-Circuits, "Datasheet: Power divider." [Online]. Available: https://www.cancer.ca/en/cancer-information/cancer-type/breast/statistics/?region=on

[61] SAMTEC, "High-speed characterization report." [Online]. Available: https://suddendocs.samtec.com/testreports/hsc-report-sma_mec2-dv_web.pdf

[62] Analog-Devices, "Datasheet: RF switch." [Online]. Available: https://www.analog.com/media/en/technical-documentation/data-sheets/hmc321a.pdf

[63] A. S. Beaverstone and N. K. Nikolova, "Modeling and design of a switched transceiver array for tissue imaging," in *IEEE MTT-S International Conference on Numerical Electromagnetic and Multiphysics Modeling and Optimization (NEMO)*. IEEE, 2015, pp. 1–3.

[64] S. Y. Semenov, R. H. Svenson, A. E. Boulyshev, A. E. Souvorov, V. Y. Borisov, Y. Sizov, A. N. Starostin, K. R. Dezern, G. P. Tatsis, and V. Y. Baranov, "Microwave tomography: Two-dimensional system for biological imaging," *IEEE Transactions on Biomedical Engineering*, vol. 43, no. 9, pp. 869–877, 1996.

[65] S. Ahsan, Z. Guo, Z. Miao, I. Sotiriou, M. Koutsoupidou, E. Kallos, G. Palikaras, and P. Kosmas, "Design and experimental validation of a multiple-frequency microwave tomography system employing the dbim-twist algorithm," *Sensors*, vol. 18, no. 10, p. 3491, 2018.

[66] M. S. Nepote, D. R. Herrera, D. F. Tapia, S. Latif, and S. Pistorius, "A comparison study between horn and vivaldi antennas for 1.5–6 ghz breast microwave radar imaging," in *The 8th European Conference on Antennas and Propagation (EuCAP 2014)*. IEEE, 2014, pp. 59–62.

[67] X. Li, S. C. Hagness, M. K. Choi, and D. W. van der Weide, "Numerical and experimental investigation of an ultrawideband ridged pyramidal horn antenna with curved launching plane for pulse radiation," *IEEE Antennas and Wireless Propagation Letters*, vol. 2, pp. 259–262, 2003.

[68] K. Moussakhani, R. K. Amineh, and N. K. Nikolova, "High-efficiency TEM horn antenna for ultra-wide band microwave tissue imaging," in *2011 IEEE International Symposium on Antennas and Propagation (APSURSI)*. IEEE, 2011, pp. 127–130.

[69] R. K. Amineh, M. Ravan, A. Trehan, and N. K. Nikolova, "Near-field microwave imaging based on aperture raster scanning with TEM horn antennas," *IEEE Transactions on Antennas and Propagation*, vol. 59, no. 3, pp. 928–940, 2010.

[70] R. K Amineh, A. Trehan, and N. K. Nikolova, "TEM horn antenna for ultra-wide band microwave breast imaging," *Progress In Electromagnetics Research*, vol. 13, pp. 59–74, 2009.

[71] M. Chiappe and G. L. Gragnani, "Vivaldi antennas for microwave imaging: Theoretical analysis and design considerations," *IEEE Transactions on Instrumentation and Measurement*, vol. 55, no. 6, pp. 1885–1891, 2006.

[72] M. Abbak, M. Akıncı, M. Çayören, and İ. Akduman, "Experimental microwave imaging with a novel corrugated vivaldi antenna," *IEEE Transactions on Antennas and Propagation*, vol. 65, no. 6, pp. 3302–3307, 2017.

[73] J. Bourqui, M. Okoniewski, and E. C. Fear, "Balanced antipodal vivaldi antenna with dielectric director for near-field microwave imaging," *IEEE Transactions on Antennas and Propagation*, vol. 58, no. 7, pp. 2318–2326, 2010.

[74] ——, "Balanced antipodal vivaldi antenna with dielectric director for near-field microwave imaging," *IEEE Transactions on Antennas and Propagation*, vol. 58, no. 7, pp. 2318–2326, 2010.

[75] S. Nikolaou, G. E. Ponchak, J. Papapolymerou, and M. M. Tentzeris, "Conformal double exponentially tapered slot antenna (detsa) on lcp for UWB applications," *IEEE Transactions on Antennas and Propagation*, vol. 54, no. 6, pp. 1663–1669, 2006.

[76] M. Ahadi, M. B. M. Isa, M. I. B. Saripan, and W. Z. W. Hasan, "Square monopole antenna for microwave imaging, design and characterisation," *IET Microwaves, Antennas & Propagation*, vol. 9, no. 1, pp. 49–57, 2015.

[77] K. Halili, M. Ojaroudi, and N. Ojaroudi, "Ultrawideband monopole antenna for use in a circular cylindrical microwave imaging system," *Microwave and Optical Technology Letters*, vol. 54, no. 9, pp. 2202–2205, 2012.

[78] M. Ojaroudi, C. Ghobadi, and J. Nourinia, "Small square monopole antenna with inverted t-shaped notch in the ground plane for UWB application," *IEEE Antennas and Wireless Propagation Letters*, vol. 8, pp. 728–731, 2009.

[79] A. Abdollahvand, A. Pirhadi, H. Ebrahimian, and M. Abdollahvand, "A compact UWB printed antenna with bandwidth enhancement for in-body microwave imaging applications," *Progress In Electromagnetics Research*, vol. 55, pp. 149–157, 2014.

[80] H. Kanj and M. Popovic, "Microwave-range broadband" dark eyes" antenna: detailed analysis and design," *IEEE Antennas and Wireless Propagation Letters*, vol. 4, pp. 262–265, 2005.

[81] X. Yun, E. C. Fear, and R. H. Johnston, "Compact antenna for radar-based breast cancer detection," *IEEE Transactions on Antennas and Propagation*, vol. 53, no. 8, pp. 2374–2380, 2005.

[82] D. Gibbins, M. Klemm, I. J. Craddock, J. A. Leendertz, A. Preece, and R. Benjamin, "A comparison of a wide-slot and a stacked patch antenna for the purpose of breast cancer detection," *IEEE Transactions on Antennas and Propagation*, vol. 58, no. 3, pp. 665–674, 2009.

[83] M. Helbig, M. Hein, R. Herrmann, M. Kmec, J. Sachs, K. Schilling, F. S. di Clemente, I. Hilger, K. Dahlke, and P. Rauschenbach, "Experimental active antenna measurement setup for UWB breast cancer detection," in *2012 IEEE International Conference on Ultra-Wideband*. IEEE, 2012, pp. 111–114.

[84] Y. L. Chow and S. Safavi-Naeini, "Active micropatch antenna device and array system," Nov. 9 1999, uS Patent 5,982,326.

[85] S. Jacobsen and O. Klemetsen, "Improved detectability in medical microwave radio-thermometers as obtained by active antennas," *IEEE Transactions on Biomedical Engineering*, vol. 55, no. 12, pp. 2778–2785, 2008.

[86] A. K. Gautam, S. Yadav, and K. Rambabu, "Design of ultra-compact UWB antenna with band-notched characteristics for mimo applications," *IET Microwaves, Antennas & Propagation*, vol. 12, no. 12, pp. 1895–1900, 2018.

[87] Keysight-Technologies, "Pathwave advanced design system (ADS)." [Online]. Available: https://www.keysight.com/ca/en/products/software/pathwave-design-software/pathwave-advanced-design-system.html

[88] Mini-Circuits, "TB-830A+ Evaluation Board." [Online]. Available: https://www.minicircuits.com/WebStore/dashboard.html?model=PMA3-83LN%2B

[89] S. Microwave, "Amphenol SMPS connector data-sheet." [Online]. Available: https://www.svmicrowave.com/sites/default/files/pdf/3811-40022-40023.PDD__0.pdf

[90] ——, "Amphenol SMPS adapter data-sheet." [Online]. Available: https://www.svmicrowave.com/sites/default/files/pdf/1138-6009.PDD_.pdf

[91] ——, "Amphenol SMPS cables data-sheet." [Online]. Available: https://www.svmicrowave.com/c-cable/frsmps-047-mssma

[92] D. M. Pozar, *Microwave Engineering*. John wiley & sons, 2011.

[93] N. K. Nikolova, "Lecture notes in devices and antennas for wireless systems."

[94] D. Rytting, "Notes network analyzer error models and calibration methods."

[95] Altium Designer, "PCB design software and tools." [Online]. Available: https://www.altium.com/

[96] G. F. Engen and C. A. Hoer, "Thru-reflect-line: An improved technique for calibrating the dual six-port automatic network analyzer," *IEEE transactions on Microwave Theory and Techniques*, vol. 27, no. 12, pp. 987–993, 1979.

Appendices

Appendix A

Paper Review

This appendix discusses the method reported in [96] and is used for error de-embedding of the high-speed connector characterized in Chapter 4. The calibration procedure starts with measuring the S-parameters of the three standards, THRU, REFLECT and LINE. These measurements are then used to calculate the scattering parameters of individual error boxes A and B. Once these errors are known, they could be calibrated out from the DUT to obtain the actual error-corrected parameters. The emergent waves b_1 and b_2 at ports 1 and 2 are related to the incident waves a_1

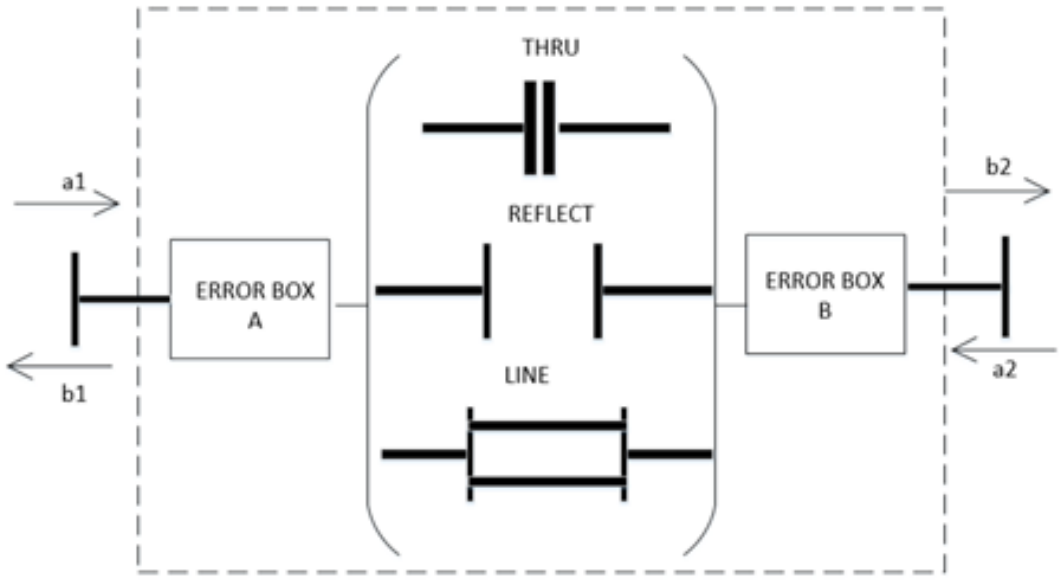

Fig. A.1. A fictitious two-ports network created using 'THRU', 'REFLECT' and 'LINE'.

and a_2 by the scattering equations

$$b_1 = S_{11}a_1 + S_{12}a_2, \tag{A.1}$$

$$b_2 = S_{21}a_1 + S_{22}a_2. \tag{A.2}$$

Dividing (A.1) by a_1 and (A.2) by a_2, we obtain the following relations

$$b_1/a_1 = S_{11} + S_{12}(a_2/a_1), \tag{A.3}$$

$$b_2/a_2 = S_{21}(a_1/a_2) + S_{22}. \tag{A.4}$$

Eliminating the ratio a_1/a_2 from the above equations we obtain,

$$w_2S_{11} + w_1S_{22} - \Delta = w_1w_2. \tag{A.5}$$

The measurements of THRU and LINE provide three independent values, while that of REFLECT provide only two, since $S_{12} = S_{21}$. Also, in this case $S_{ii} = w_i$ and $i = 1, 2$.

In order to determine the scattering parameters of the error boxes A and B, it is useful to make use of wave cascading matrix or scattering transfer matrix which provides T-parameters. It relates the emergent and incident waves as follows:

$$\begin{bmatrix} b_1 \\ a_1 \end{bmatrix} = \frac{1}{S_{21}} \begin{bmatrix} -\Delta & S_{11} \\ -S_{22} & 1 \end{bmatrix} \begin{bmatrix} b_2 \\ a_2 \end{bmatrix}, \Delta = S_{11}S_{22} - S_{12}S_{21}. \tag{A.6}$$

Here, $\frac{1}{S_{21}} \begin{bmatrix} -\Delta & S_{11} \\ -S_{22} & 1 \end{bmatrix}$ is the wave cascading matrix.

The following nomenclature will be used throughout the discussion:

- R_a: wave cascading matrix (T-matrix) of error box A.
- R_b: wave cascading matrix of error box B.

- R_T: wave cascading matrix of the THRU standard.
- R_L: wave cascading matrix of the LINE standard.
- T : wave cascading matrix of the THRU measurement.
- L : wave cascading matrix of the LINE measurement.

Using equation (A.6), we can write the cascading matrix for error box A and error box B as follows:

$$R_a = \frac{1}{S_{21a}} \begin{bmatrix} -\Delta_a & S_{11a} \\ -S_{22a} & 1 \end{bmatrix}, \Delta_a = S_{11a}S_{22a} - S_{12a}S_{21a}, \tag{A.7}$$

and,

$$R_b = \frac{1}{S_{21b}} \begin{bmatrix} -\Delta_b & S_{11b} \\ -S_{22b} & 1 \end{bmatrix}, \Delta_b = S_{11b}S_{22b} - S_{12b}S_{21b}. \tag{A.8}$$

Considering the THRU as the reference plane, T is the resultant cascade matrix of error box A, the THRU standard and error box B, and is given as,

$$T = R_a R_T R_b \tag{A.9}$$

In practice, T is the matrix that is obtained from the measurements of the *S*-parameters of the THRU standard (when it is used as DUT) using the VNA. Note that the actual wave cascading matrix of the THRU standard is known and is given as

$$R_T = \begin{bmatrix} 1 & 0 \\ 0 & 1 \end{bmatrix}. \tag{A.10}$$

Substituting this matrix in (A.9), we obtain

$$T = R_a R_b \tag{A.11}$$

Next, we consider the LINE connection for which the resultant cascading matrix after the measurement is given as

$$\mathrm{L} = \mathrm{R_a R_L R_b}, \tag{A.12}$$

and here assuming the line is non-reflecting,

$$\mathrm{R_L} = \begin{bmatrix} e^{-\gamma l} & 0 \\ 0 & e^{\gamma l} \end{bmatrix}. \tag{A.13}$$

γ and l represent, the propagation constant and length of the line standard respectively. Rearranging the expression in (A.11), error box B can be determined as follows,

$$\mathrm{R_b} = \mathrm{R_a}^{-1}\mathrm{T}. \tag{A.14}$$

Substituting (A.14) in (A.12) and rearranging, we obtain

$$\mathrm{HR_a} = \mathrm{R_a R_L}, \tag{A.15}$$

where,

$$\mathrm{H} = \mathrm{LT}^{-1}. \tag{A.16}$$

The matrix H is completely known and can be found from the parameters of the TRHU and LINE measurements. Representing matrix H and matrix $\mathrm{R_a}$ in terms of their cascading parameters we get,

$$\mathrm{H} = \begin{bmatrix} h_{11} & h_{12} \\ h_{21} & h_{22} \end{bmatrix}, \tag{A.17}$$

and

$$\mathrm{R_a} = \begin{bmatrix} r_{11a} & r_{12a} \\ r_{21a} & r_{22a} \end{bmatrix} \tag{A.18}$$

or

$$\mathrm{R_a} = \mathrm{r_{22a}} \begin{bmatrix} a & b \\ c & 1 \end{bmatrix}. \tag{A.19}$$

Here, $a = r_{11a}/r_{22a}$, $b = r_{12a}/r_{22a}$, and $c = r_{21a}/r_{22a}$ Representing cascading matrix of error box B similar to that of error box A, we obtain,

$$\mathrm{R_b} = \mathrm{r_{22b}} \begin{bmatrix} \alpha & \beta \\ \delta & 1 \end{bmatrix} \tag{A.20}$$

and $\alpha = r_{11b}/r_{22b}, \beta = r_{12b}/r_{22b}$, and $\delta = r_{21b}/r_{22b}$. Expanding (A.15) we obtain a set of following equations,

$$h_{11}r_{11a} + h_{12}r_{21a} = r_{11a}e^{-\gamma l} \tag{A.21}$$

$$h_{21}r_{11a} + h_{22}r_{21a} = r_{21a}e^{-\gamma l} \tag{A.22}$$

$$h_{11}r_{12a} + h_{12}r_{22a} = r_{12a}e^{\gamma l} \tag{A.23}$$

$$h_{21}r_{12a} + h_{22}r_{22a} = r_{22a}e^{\gamma l} \tag{A.24}$$

To continue, take ratio of (A.21) to (A.22) and (A.23) to (A.24). We obtain the following expressions:

$$h_{21}(r_{11a}/r_{21a})^2 + (h_{22} - h_{11})(r_{11a}/r_{21a}) - h_{12} = 0 \tag{A.25}$$

$$h_{21}(r_{12a}/r_{22a})^2 + (h_{22} - h_{11})(r_{12a}/r_{22a}) - h_{12} = 0 \tag{A.26}$$

Also, taking ratio of (A.21) to (A.24) gives

$$e^{2\gamma l} = \frac{h_{21}(r_{12a}/r_{22a}) + h_{22}}{h_{12}(r_{21a}/r_{11a}) + h_{11}}. \tag{A.27}$$

As can be seen from (A.25) and (A.26), the ratios (r_{11a}/r_{21a}) and (r_{12a}/r_{22a}) are roots of the same quadratic equations and the coefficients are parameters of the wave cascading matrix of error box A. Also, we can obtain the propagation constant of LINE

from (A.27). The next problem is to identify which root represents a/c or b.

$$b_1 = r_{12a}\left(\frac{r_{11a}}{r_{12a}}a_2 + b_2\right) \tag{A.28}$$

$$a_1 = r_{22a}\left(\frac{r_{21a}}{r_{22a}}a_2 + b_2\right) \tag{A.29}$$

In most measurement systems it is desirable to have a response nominally proportional to wave amplitude b_2 incident upon the item under test. This can be achieved if $|r_{21a}/r_{22a}| \ll 1$. Further it is required that rest of the response is tied nominally to a_2 which requires $|r_{11a}/r_{12a}| \gg 1$. So we obtain,

$$\left|\frac{r_{11a}}{r_{12a}}\right| > \left|\frac{r_{21a}}{r_{22a}}\right| \tag{A.30}$$

This in turn results in,

$$|b| < |a/c|. \tag{A.31}$$

To continue, the reflection coefficient w_1 at the detector plane for error port A is related to the reflection coefficient of the load $Gamma_l$ by

$$w_1 = \frac{a\Gamma_l + b}{c\Gamma_l + 1} \tag{A.32}$$

We have already obtained the values of b and a/c. Thus, evaluating a will complete the determination of error box A. Rearranging (A.32) we obtain,

$$a = \frac{w_1 - b}{\Gamma(1 - w_1 c/a)} \tag{A.33}$$

If $Gamma_l$ is known a can be determined from (A.33) as all other parameters are known. To calculate the rest of the unknown we can continue as follows

$$g\begin{bmatrix} d & e \\ f & 1 \end{bmatrix} = r_{22a}r_{22b}\begin{bmatrix} a & b \\ c & 1 \end{bmatrix}\begin{bmatrix} \alpha & \beta \\ \delta & 1 \end{bmatrix} \tag{A.34}$$

Here d, e, f, and g correspond to a, b, c, and r_{22a} in R_a. Pre-multiplying (A.34) by ${R_a}^{-1}$ and expanding, we obtain the following relationships,

$$\delta = \frac{f - d(c/a)}{1 - e(c/a)} \tag{A.35}$$

$$\beta/\alpha = \frac{e - b}{d - bf} \tag{A.36}$$

and

$$a\alpha = \frac{d - bf}{1 - e(c/a)} \tag{A.37}$$

The values of b and c/a are already known, and d, e, f, and g can be obtained from R_t, thus β/α, δ, and $a\alpha$ can be calculated from (A.35)-(A.35). For error box B, α can be obtained in a similar manner as a in (A.33),

$$\alpha = \frac{w_2 + \delta}{\Gamma(1 + w_2(\beta/\alpha)} \tag{A.38}$$

where the reversed signs and interchange between the roles of β and δ are due to the reversed direction associated with "error box B". Eliminating Γ between (A.33) and (A.38) we obtain

$$a/\alpha = \frac{(w_1 - b)(1 + w_2(\beta/\alpha))}{(w_2 + \delta)(1 - w_1(c/a))} \tag{A.39}$$

Solving (A.37) and (A.39)

$$a = \sqrt{\frac{(w_1 - b)(1 + w_2(\beta/\alpha))(d - bf)}{(w_2 + \delta)(1 - w_1(c/a))(1 - e(c/a))}} \tag{A.40}$$

and

$$\alpha = \frac{(d - bf)}{a(1 - e(c/a))} \tag{A.41}$$

From the above equations, we can observe that the need to know Γ_l has been eliminated, and the errors can be calculated using only the S-parameter measurements.

Appendix B

MATLAB Code for Error De-embedding

```
% STEP 1: reading data from the measured thru parameters
thru = sparameters('T_S11.s2p');
frequency = thru.Frequencies;% extract the frequencies from data
freq= frequency/1e9;
s11t = rfparam(thru,1,1); % extracting s11 from the data
s12t = rfparam(thru,1,2); % extracting s12 from the data
s21t = rfparam(thru,2,1); % extracting s21 from the data
s22t = rfparam(thru,2,2); % extracting s22 from the data

% STEP 2; reading data from measured line parameters
line = sparameters('L_S11.s2p');
s11l = rfparam(line,1,1);
s12l = rfparam(line,1,2);
s21l = rfparam(line,2,1);
s22l = rfparam(line,2,2);

% STEP 3; reading data from measured reflect parameters
```

```
reflect = sparameters('R_S11.s2p');
s11r = rfparam(reflect,1,1);
s12r = rfparam(reflect,1,2);
s21r = rfparam(reflect,2,1);
s22r = rfparam(reflect,2,2);

% STEP 4: reading data of DUT
dut = sparameters('center_trace.s2p');
s11d = rfparam(dut,1,1);
s12d = rfparam(dut,1,2);
s21d = rfparam(dut,2,1);
s22d = rfparam(dut,2,2);
s11d_db= 20*log10(abs(s11d));
s12d_db= 20*log10(abs(s12d));
s21d_db= 20*log10(abs(s21d));
s22d_db= 20*log10(abs(s22d));

% STEP 5: Creating T matrix for thru standard measurement
T11 = -(s11t.*s22t - s12t.*s21t)./s21t;
T12 =  s11t./s21t;
T21 = -s22t./s21t;
T22 =  1 ./s21t;

% STEP 6: Creating T matrix for line standard measurement
L11 = -(s11l.*s22l - s12l.*s21l)./s21l;
L12 =  s11l./s21l;
L21 = -s22l./s21l;
L22 =  1 ./s21l;

% STEP 7: Creating T matrix for reflect standard measurement
R11 = -(s11r.*s22r - s12r.*s21r)./s21r;
```

```
R12 =  s11r./s21r;
R21 = -s22r./s21r;
R22 =  1 ./s21r;

% STEP 8: Creating T matrix for DUT
DUT11 = -(s11d.*s22d - s12d.*s21d)./s21d;
DUT12 =  s11d./s21d;
DUT21 = -s22d./s21d;
DUT22 =  1 ./s21d;

nfreq=length(freq);
for n=1:nfreq
    R_T= [T11(n) T12t(n); T21(n) T22(n)];
    R_L= [L11(n) L12(n); L21(n) L22(n)];
    %Rt = inv(R_T);
    H= Rd*inv(Rt);
    A= H(2,1);
    B= H(2,2)-H(1,1);
    C= -H(1,2);
    K1=(-B+sqrt(B^2-4*A*C))/(2*A);
    K2=(-B-sqrt(B^2-4*A*C))/(2*A);

    %determining the correct root
    if abs(K1)<abs(K2)
        b=K1;
        c_a=1/K2;% c/a
    else
    %if abs(K2)<abs(K1)
        b=K2;
        c_a=(1/K1);
    end
```

```
  % Calculates the propogation constant of the LINE standerd.
gammal(n)= 0.5*(log(T(2,1)*b+H(2,2)/H(1,2)*c_a+H(1,1)));

  % Calculating a
  w1= s11r(n);
  w2= s22r(n);

  d= T11(n)/T22(n);
  e= T12(n)/T22(n);
  f= T21(n)/T22(n);
  g= T22(n);

  %determining the variables of error box B
  delta= (f-d*c_a)/(1-e*c_a);
  beta_alpha=(e-b)/(d-(b*f));% beta/alpha
  aalpha= (d-(b*f))/(1-e*c_a); % a*alpha
  Numerator=(w1-b)*(1+w2*beta_alpha)*(d-b*f);
  Denominator= (w2+delta)*(1-w1*c_a)*(1-e*c_a);
  a= sqrt(Numerator/Denominator);
  %a_a=-a;
  c= c_a*a;
  Refl_coeff(n)= (w1-b)/(a-c*w1);
  alpha= (d-b*f)/(a*(1-e*c_a));
  beta = beta_alpha*alpha;

  r22p22= T11(n)/(a*alpha+b*delta);
  Inv_Ra= [1 -b; -c a];
  Inv_Rb= [1 -beta; -delta alpha];

  % Matrix of measured dut parameters
  R_M= [DUT11(n) DUT12(n); DUT21(n) DUT22(n)];
```

```
    x= a-(b*c);
    y= alpha-(beta*delta);
    % defining the actual matrix
    R_dut= (1/(r22p22*x*y))*Inv_Ra*R_M*Inv_Rb; % extracted $T$-parameters

    %De-embedding the S parameters of the DUT from its T matrix
    S11_d(n)= R_dut(1,2)/R_dut(2,2);
    S12_d(n)= (R_dut(1,1)-(R_dut(1,2)*R_dut(2,1)))/R_dut(2,2);
    S21_d(n)= 1/(R_dut(2,2));
    S22_d(n)= -R_dut(2,1)/(R_dut(2,2));

     % De-embedded S parameters
     S_dut= [S11_d S12_d; S21_d S22_d];
end
figure(1)
plot(freq,s11d_db)
hold on
plot(freq,20*log10(abs(S11_d)))
xlabel('Frequency (GHz)')
ylabel('Magnituge (dB)')
%title('S-Parameters of high speed connector')
grid on

figure(2)
plot(freq,s21d_db)
hold on
plot(freq,20*log10(abs(S21_d)))
xlabel('Frequency (GHz)')
ylabel('S21 Magnituge (dB)')
grid on
```